HHS Public Access

Author manuscript

Nat Neurosci. Author manuscript; available in PMC 2019 January 23.

Published in final edited form as:

Nat Neurosci. 2018 August ; 21(8): 1084–1095. doi:10.1038/s41593-018-0198-x.

PARALLEL CIRCUITS FROM THE BED NUCLEI OF STRIA TERMINALIS TO THE LATERAL HYPOTHALAMUS DRIVE OPPOSING EMOTIONAL STATES

William J. Giardino[1], **Ada Eban-Rothschild**[1,2], **Daniel J. Christoffel**[1], **Shi-Bin Li**[1], **Robert C. Malenka**[1], and **Luis de Lecea**[1,*]

[1]Department of Psychiatry & Behavioral Sciences, Stanford University, Stanford, CA, USA 94305

[2]Current address: Department of Psychology, University of Michigan, Ann Arbor, MI, USA 48109

Abstract

Lateral hypothalamus (LH) neurons containing the neuropeptide hypocretin (Hcrt; orexin) modulate affective components of arousal, but their relevant synaptic inputs remain poorly defined. Here, we identified inputs onto LH neurons that originate from neuronal populations in the bed nuclei of stria terminalis (BNST; a heterogeneous region of extended amygdala). We characterized two non-overlapping LH-projecting GABAergic BNST subpopulations that express distinct neuropeptides (corticotropin-releasing factor; *Crf*, and cholecystokinin; *Cck*). To functionally interrogate BNST→LH circuitry, we used tools for monitoring and manipulating neural activity with cell-type-specific resolution in freely-behaving mice. We found that *Crf*-BNST and *Cck*-BNST neurons respectively provide abundant and sparse inputs onto *Hcrt*-LH neurons, display discrete physiological responses to salient stimuli, drive opposite emotionally valenced behaviors, and receive different proportions of inputs from upstream networks. Together, our data provide an advanced model for how parallel BNST->`LH pathways promote divergent emotional states via connectivity patterns of genetically defined, circuit-specific neuronal subpopulations.

INTRODUCTION

Appropriate responding to aversive and rewarding stimuli is essential for survival, and subcortical neural systems for regulating emotions are evolutionarily conserved. The precise mechanisms underlying approach and avoidance behavior are beginning to be uncovered, with efforts focused on the intricate connectivity of the lateral hypothalamus (LH)[1,2]. The LH receives dense synaptic inputs from the amygdala- a brain region critical for emotional processing. Multiple distinct cell types are co-mingled in the LH, and posterodorsal LH

*Corresponding author: llecea@stanford.edu.

AUTHOR CONTRIBUTIONS

W.J.G. and L.d.L. conceived and designed the studies. W.J.G. and A.E.-R. and D.J.C. and S.-B. L. performed experiments. W.J.G. and D.J.C. analyzed data. R.C.M. provided equipment and resources, W.J.G. wrote the manuscript with contributions from A.E.-R., D.J.C., and L.d.L.

COMPETING FINANCIAL INTERESTS

The authors declare no competing financial interests.

neurons expressing the neuropeptide hypocretin (Hcrt[3]; also known as orexin[4]) are particularly important for motivated behaviors[5–7]. Hcrt-LH neurons project throughout the brain, acting via Hcrt receptor (HcrtR) signaling to facilitate arousal (wakefulness) and enable behavioral state transitions[8,9]. Yet, the precise relationships between Hcrt-LH activity and emotional behavior remain elusive. HcrtR signaling has been hypothesized to promote both negative[10,11] and positive[12,13] emotional states, but a nuanced theory for how Hcrt-LH neurons process oppositely-valenced stimuli remains under development.

Hcrt-LH neurons receive physiological signals from wide-ranging brain circuits[14,15], and can be activated by neuropeptide modulators[16,17]. In particular, inputs to the LH originating from the extended amygdala may govern complex behavioral responses to emotional stimuli. We focused on the bed nuclei of stria terminalis (BNST), a heterogeneous collection of neuropeptide-enriched extended amygdala cell groups that project to the LH and are sufficient to drive emotion-related behaviors[1,18]. The complex cellular organization of the BNST historically presented a challenge for functional dissection of these numerous anatomical divisions and subnuclei[19]. Multiple hypotheses now exist for how the BNST regulates emotional behavior, including division of neurons by classical neurotransmission type[20], axonal targets[18], and interneuron vs. projection neuron types[21]. However, these ideas minimize the potential importance of the extensive molecular heterogeneity of the BNST.

To dissect BNST→LH circuitry with genetically-defined and pathway-specific resolution, we used viral-based Cre-inducible methods for monitoring endogenous calcium (Ca^{2+}) signals with fiber photometry[22], manipulating neural activity with optogenetics[23] and chemogenetics[24], mapping monosynaptic connections with modified rabies viral tracing[25], and assessing synaptic connectivity with *ex vivo* slice electrophysiology. We identified two spatially-segregated GABAergic BNST subpopulations that 1) express distinct neuropeptide markers, 2) differentially innervate defined LH subpopulations, 3) display different patterns of salient stimuli-induced Ca^{2+} activity, 4) receive afferent input from distinct upstream networks, and 5) drive oppositely-valenced approach and avoidance behaviors, in part via their axonal outputs to LH. Thus, we provide a framework for how multiple genetically-segregated GABAergic/neuropeptide BNST cell types promote opposing emotional states via divergent connectivity with distinct LH subpopulations.

RESULTS

Hcrt-LH and *LepRb*-LH neurons: physiology and behavior

To establish selective Hcrt-LH targeting, we developed a novel knock-in IRES Cre mouse line (*Hcrt*-Cre; Fig.S1a-b). Following intra-LH delivery of Cre-inducible fluorescent-labeled adeno-associated virus (AAV), we found that >90% of viral-expressing neurons were Hcrt-positive, indicative of specific recombinase activity in the Hcrt-LH field (Fig. 1a, S1c-d). To assess whether *Hcrt*-LH neurons are activated by salient stimuli in real time, we used *in vivo* fiber photometry to record Ca^{2+} signals following exposure to ethologically-relevant odorant stimuli. We transduced *Hcrt*-LH neurons with the GFP-based Ca^{2+} indicator GCaMP6, implanted fiberoptics above the LH (Fig. 1a), and habituated mice to the system for freely-moving trials in their homecages[26]. Relative to baseline pre-stimulus recordings, homecage introduction of any object (including no-scent saline control stimuli) increased *Hcrt*-LH

Ca^{2+} activity, indicative of a general response to environmental stimuli (Fig. 1b). However, relative to control stimuli, *Hcrt*-LH GCaMP6 fluorescence was elevated following presentation of predator odor (trimethyl-3-thiazoline; TMT/fox urine) (Fig. 1b, S1e). No significant fluorescence changes were detected during recordings of non-GCaMP6-expressing *Hcrt*-LH-GFP neurons in control mice (Fig. S1f). Together, we observed that, although *Hcrt*-LH neurons display increased Ca^{2+} activity to stimuli in general, these neurons are especially sensitive to negative emotionally-valenced stimuli. These results are supported by existing data showing increased "orexin-LH" Ca^{2+} activity in response to negative emotionally-valenced stimuli of additional sensory domains (air puff and immobilization stress[14]).

We next performed fiber photometry recordings from LH neurons marked by the leptin receptor (*LepRb*-Cre), a non-overlapping population intermingled with Hcrt-LH neurons (Fig. 1c). We chose *LepRb*-LH neurons because our group previously showed that they regulate the neuroendocrine and behavioral stress response via GABAergic inhibition of *Hcrt*-LH neurons[27]. Therefore, we hypothesized that increased *Hcrt*-LH Ca^{2+} may require a suppression of GABAergic input from *LepRb*-LH neurons. Consistent with this premise, we found that GCaMP6-expressing *LepRb*-LH neurons (Fig. S2a) showed an overall reduction in activity upon stimuli presentation (Fig. 1d). In particular, female mouse urine and predator odor resulted in reduced Ca^{2+} activity in *LepRb*-LH neurons, relative to *Hcrt*-LH neurons (Fig. 1e).

Given the literature implicating Hcrt-LH activation in both aversion[10,11,17] and reward[12,13], we used optogenetic stimulation to clarify the hedonic valence associated with physiological excitation of *Hcrt*-LH vs. *LepRb*-LH neurons. For photostimulation, we transduced *Hcrt*-LH neurons with channelrhodopsin-2 tagged with enhanced yellow fluorescent protein (ChR2-eYFP; or eYFP-only control virus), and implanted fiberoptics above the LH. We found >90% of ChR2-eYFP positive cells were Hcrt-positive (Fig. 1f, S1d). We analyzed behavior of mice undergoing the real-time place test (RTPT), in which photostimulation (no-light control, or 10ms pulses of 473nm light at 5Hz or 10Hz) is paired with one counterbalanced side of the RTPT apparatus (Fig. 1g). Compared to control mice that typically spent equivalent time on either side of the apparatus, *Hcrt*-LH-ChR2 mice avoided the photostimulation-paired side (Fig. 1h), suggesting that photostimulation of *Hcrt*-LH neurons produced an aversive, negative emotional state. Relative to controls, *Hcrt*-LH-ChR2 mice displayed decreased time spent per entry to the stimulation side, with no differences in number of entries to the stimulation side, suggesting that potential locomotor changes are unlikely to account for *Hcrt*-LH-ChR2 avoidance (Fig. S1g-h).

To determine the necessity of HcrtR signaling for *Hcrt*-LH-ChR2 aversion, we tested mice following pretreatment with the dual HcrtR antagonist MK6096 (Filorexant[28,29]). MK6096 administration blocked RTPT avoidance, suggesting that HcrtR signaling is required for *Hcrt*-LH-ChR2 aversion (Fig. S1i). Most *Hcrt*-LH neurons co-express dynorphin[13], the kappa opioid receptor (KOR) endogenous ligand, so we tested the ability of pharmacological KOR blockade to alter *Hcrt*-LH-ChR2 aversion. Following pretreatment with KOR antagonist norbinaltorphimine (norBNI), 10Hz photostimulation produced RTPT avoidance,

suggesting that norBNI-sensitive KOR signaling may not be required for *Hcrt*-LH-ChR2 aversion (Fig. S1j).

In contrast to the aversive nature of *Hcrt*-LH activation, photostimulation of *LepRb*-LH neurons produced real-time place preference, indicating that *LepRb*-LH activation is rewarding (Fig. 1i). Relative to controls, *LepRb*-LH-ChR2 mice displayed increased time spent per entry to the stimulation side, with no differences in the number of entries to the stimulation side, suggesting that potential locomotor changes related to *LepRb*-LH photostimulation are unlikely to account for *LepRb*-LH-ChR2 preference (Fig. S2b-c). In summary, we found that *Hcrt* and *LepRb* neurons displayed unique salient stimuli-induced Ca^{2+} activity profiles, and that *Hcrt* and *LepRb* photostimulation generated oppositely-valenced avoidance and approach behaviors.

Hcrt and *LepRb*: mapping inputs onto LH subpopulations

Given the limited understanding of the *Hcrt*-LH neurocircuitry of negatively-valenced emotional states, we sought to elucidate the upstream networks that drive and regulate *Hcrt*-LH activity. To label upstream cells making direct synapses onto *Hcrt*-LH neurons, we used the glycoprotein-deleted rabies (RV*dG*-GFP) monosynaptic tracing strategy[25]. Following identification of double-labeled mCherry+/GFP+ starter cells (Fig. 1j), whole-brain analyses identified major afferent inputs from forebrain, hypothalamus, amygdala, midbrain, and brainstem (Fig. 1k). Quantitative analyses highlighted the BNST as the primary non-LH source of inputs onto *Hcrt*-LH neurons (10.7% of 11,489 cells from n=4 mice; Fig. 1l).

To compare our results to non-Hcrt-LH neurons, we performed the RV*dG*-GFP strategy in *LepRb*-Cre mice (Fig. 1l, S2d-e). Analogous to *Hcrt*-LH studies, we identified the BNST as an abundant source of inputs onto *LepRb*-LH neurons (9.6% of 5,360 cells from n=3 mice). Compared to *LebRb*-LH, *Hcrt*-LH neurons received less abundant input from the LH itself, but more abundant input from the paraventricular hypothalamus (PVN) and ventral tegmental area (VTA) (Fig. 1l). These data indicate that discrete LH cell types share a major input source (BNST), but also receive differentially abundant input from other sources.

Neurochemical identification of LH-projecting BNST subpopulations

Next, we characterized the BNST neurons making direct synapses onto LH neurons (Fig. 2a). To delineate BNST subdivisions, we performed cytoarchitectural analyses of DAPI-labeled coronal slices, relying on anatomical distinctions defined by L.W. Swanson, Paxinos & Watson, the Allen Brain Institute, and others[19,30–34]. We found RV*dG*-GFP+ cells throughout anterior (+0.60 to +0.12 mm from bregma) and posterior (+0.12 to −0.36 mm from bregma) BNST divisions in both *Hcrt* and *LepRb* mice (Fig. 2b-c). Compared to *LepRb* mice, RVdG-GFP+ cells in *Hcrt* mice were more concentrated in lateral BNST, relative to medial BNST (Fig. 2b-c).

To select cell types for dissecting BNST→LH connectivity, we screened the BNST for markers that distinguished between lateral vs. medial BNST, focusing on the dorsal BNST in the anterior-middle range of the rostrocaudal axis, analogous to the anterodorsal (ad)BNST[18]. We crossed several Cre driver mouse lines with the Cre-inducible tdTomato (LSL-*Ai14*) reporter mouse line, and visualized tdTomato expression in BNST (Fig. S3a).

Neurons expressing genes encoding the vesicular GABA transporter (*Vgat*) or the neuropeptide substance P (tachykinin; *Tac1*) were in both lateral and medial adBNST, whereas neurons expressing the gene encoding the vesicular glutamate transporter *Vglut2* were absent from adBNST, except in the bed nucleus of the anterior commissure. Three markers (*Drd1*; dopamine receptor-1, *Crf;* corticotropin-releasing factor, and *Pdyn;* prodynorphin) preferentially labeled laterally-enriched adBNST subpopulations, including cells in the juxtacapsular (jc) and oval (ov) subnuclei. These anterodorsolateral (adl)BNST subgroups formed contiguous populations that extended caudally (and ventrally) to form the lateral division of the posterior BNST (posterolateral; plBNST). Unlike lateral BNST markers, *Cck* (cholecystokinin) labeled medially-restricted BNST neurons (Fig. S3a). We found dorsomedial (dm)BNST *Cck* neurons beginning anteriorly at +0.20 mm from bregma that comprised a contiguous population extending caudally (and ventrally) to form the medial division of the posterior BNST (posteromedial; pmBNST), classically known as the principal nucleus[35].

We chose *Crf and Cck* as markers of laterally-enriched vs. medially-restricted BNST neurons because they encode proteins (CRF and CCK) that are peptide neuromodulators with documented roles in driving emotional behavior and altering LH neuron activity[16,17]. CRF is a well-established lateral BNST marker, and *Crf*-BNST neurons modulate anxiety, fear, and addiction-related behaviors[21,36]. Following the screen of genetically-encoded markers, we visualized CRF and CCK neuropeptide immunostaining in adult mice, verifying lateral vs. medial BNST expression patterns at the protein level (Fig. 2d).

In *Hcrt*-LH-RV*dG* mice, we identified more RV*dG*-GFP+ BNST neurons co-expressing CRF relative to CCK, demonstrating that *Hcrt*-LH neurons receive more abundant inputs from CRF vs. CCK neurons (Fig. 2e-f). RV*dG*-GFP+ BNST neurons in *Hcrt*-LH mice also comprised a larger percentage of the CRF-BNST population, relative to the CCK-BNST population (Fig. 2f). CRF and CCK neurons together comprised 25% of *Hcrt*-LH-RV*dG*-GFP+ BNST neurons, suggesting the existence of additional BNST→*Hcrt*-LH subpopulations. In *LepRb*-LH-RV*dG* mice, we also identified CRF+ and CCK+ RV*dG*-GFP + neurons, suggesting that *LepRb*-LH neurons receive both CRF and CCK inputs (Fig. S3b-c).

Based on differential connectivity of CRF vs. CCK onto *Hcrt* neurons, we selected *Crf* and *Cck* Cre mouse lines to dissect these genetically-segregated BNST→LH pathways. To validate lines for BNST manipulations, we performed immunostaining for CRF and CCK in tdTomato reporter mice (Fig. S3d-e). *Crf*-Ai14 and *Cck*-Ai14 reporter expression corresponded closely with CRF and CCK peptide expression, respectively (Fig. S3d). *Vgat*-Ai14 and *Vglut2*-Ai14 analyses revealed that CRF and CCK cells are primarily GABAergic, and not glutamatergic (Fig. S3d). *Drd1*-Ai14 and *Tac1*-Ai14 analyses revealed modest co-expression with CRF (Fig. S3e), suggesting that CRF represents one of many partially-overlapping BNST→LH subpopulations. To address cross-overlap between lateral vs. medial subgroups, we observed that *Crf*-Ai14 was not co-expressed with CCK, and *Cck*-Ai14 was not co-expressed with CRF. Thus, we established *Crf*/CRF and *Cck*/CCK as two non-overlapping lateral vs. medial GABAergic BNST subpopulations (Fig. S3d).

Crf and *Cck* BNST neurons: physiology and behavior

To evaluate the response of BNST subpopulations to salient stimuli, we measured Ca^{2+} activity from *Crf* and *Cck* neurons expressing GCaMP6. Due to the abundance of lateral BNST→*Hcrt*-LH connections, we hypothesized that *Crf*-BNST neurons would display greater sensitivity to aversive rather than appetitive stimuli. Relative to control stimuli, *Crf*-BNST-GCaMP6 fluorescence was increased by predator odor, but not by other stimuli (Fig. 3a). In contrast, *Cck*-BNST-GCaMP6 fluorescence levels in male mice were specifically increased an appetitive odorant stimulus: urine from mice of the opposite sex[37] (Fig. 3b). Direct comparisons of genetically-defined BNST activity revealed greater response of *Crf* vs. *Cck* neurons to predator odor, and greater response of *Cck* vs. *Crf* neurons to female mouse urine (Fig. 3c). The distinct responses of lateral vs. medial BNST subpopulations to oppositely-valenced stimuli corresponded to their differential connectivity onto *Hcrt*-LH neurons (Fig. 2), leading us to hypothesize that *Crf* and *Cck* drive opposing emotional states via divergent LH connectivity.

To determine the hedonic valence associated with activation of *Crf* and *Cck* subpopulations, we performed optogenetic stimulations. First, we used slice electrophysiological recordings of ChR2-expressing BNST cell bodies to validate spike fidelity to blue light stimulation (Fig. 3d-e). Based on abundant *Crf*-BNST→*Hcrt*-LH connectivity, and distinct Ca^{2+} responses of *Crf* vs. *Cck* BNST neurons, we hypothesized that *Crf* and *Cck* stimulations would elicit behavioral avoidance and approach, respectively. Relative to controls, *Crf*-BNST-ChR2 photostimulation produced avoidance of the stimulation-paired side (Fig. 3d), suggesting that *Crf*-BNST activation is aversive. *Cck*-BNST-ChR2 photostimulation produced preference for the stimulation-paired side (Fig. 3e), suggesting that *Cck*-BNST activation is rewarding. Analogous to previous studies[1,20], photostimulation of *Vgat*-BNST neurons produced preference (Fig. S4a-b). This suggests that, while activation of a non-specific population of GABAergic *Vgat*-BNST neurons is rewarding, stimulation of a laterally-enriched subset of GABAergic *Vgat*-BNST neurons (like *Crf*) can be aversive. To further test this, we photostimulated additional laterally-enriched (*Drd1*) and medially-restricted (*Six3*) BNST subpopulations in the RTPT, and observed avoidance and preference, respectively (Fig. S4c-f), supporting findings from *Crf* and *Cck* experiments. Together, these results demonstrate that the *Vgat*-BNST population consists of genetically-defined and spatially-segregated subpopulations that have either similar or distinct behavioral effects, relative to the global *Vgat*-BNST population.

Crf and *Cck*: mapping inputs onto BNST subpopulations

In considering that *Crf* and *Cck* displayed differential connectivity with *Hcrt*-LH neurons (Fig. 2), distinct Ca^{2+} responses to salient stimuli (Fig. 3a-c), and divergent behaviors upon photostimulation (Fig. 3d-e), we hypothesized that these cells receive synaptic inputs from distinct upstream circuits. Thus, we used the modified rabies strategy in the BNST of *Crf* and *Cck* mice. *Crf* and *Cck* BNST starter cells were restricted to lateral and medial BNST, respectively (Fig. 3f).

We first examined intra-BNST connectivity by counting RV*dG*-GFP+ cells throughout all BNST subdivisions (excluding mCherry+/GFP+ starter cells). We discovered that *Crf*-BNST

neurons received a larger share of inputs from adlBNST, relative to *Cck*-BNST neurons (Fig. 3g-h). Conversely, *Cck*-BNST neurons received a larger share of inputs from admBNST and pmBNST. Thus, although we observed substantial BNST→BNST local connectivity, these connections were more abundant *within* the same BNST subdivision rather than *across* different BNST subdivisions (Fig. 3g-h).

Brainwide counts of RV*dG*-GFP+ cells outside the BNST identified the medial amygdala (MeA) as the primary input source onto *Crf*-BNST neurons (6.8% of 3,473 cells from n=4 mice), followed by medial preoptic area (MPoA), PVN, and central nucleus of amygdala (CeA) (Fig. 3i-j). Reminiscent of *Crf*-BNST neurons, *Cck*-BNST neurons also received their most abundant inputs from the MeA and MPoA. However, compared to *Crf*, *Cck* neurons received more abundant input from MeA, and less abundant input from PVN and anteroventral periventricular nucleus/ventromedial preoptic area (AVPV/VMPO) (Fig. 3i-j).

PVN was the only identified region that provided more abundant input onto *Hcrt* vs. *LepRb* neurons, as well as more abundant input on *Crf* vs. *Cck* neurons (Fig. 1l, Fig. 3j). PVN neurons containing CRF are essential for orchestrating the hypothalamic-pituitary-adrenal axis and associated stress-coping behaviors[38]. Therefore, we hypothesized that *Crf*-PVN neurons are a common node in stress/avoidance *Crf*-BNST→*Hcrt*-LH circuitry. To test this, we photostimulated *Crf*-PVN neurons in the RTPT and observed behavioral avoidance (Fig S4g-h), indicating that strong PVN inputs onto *Hcrt*-LH and *Crf*-BNST neurons manifest behaviorally. We propose that these circuits consist of highly interconnected nodes (*Crf*-PVN, *Crf*-BNST, *Hcrt*-LH) that work in feedforward fashion to drive avoidance behaviors in response to stressful stimuli.

Chemogenetic self-stimulation of *Crf* and *Cck* neurons

To determine the emotional states associated with genetically-defined BNST intracellular G-protein signaling, we used excitatory (hM3Dq) designer receptors exclusively activated by designer drugs (DREADDs; Fig. 4a). Slice electrophysiological recordings validated CNO-evoked spiking and increased membrane potential (Fig. 4b). To measure chemogenetic self-stimulation, mice expressing hM3Dq-DREADDs (or control virus) in BNST neurons were tested for voluntary consumption of the DREADD ligand clozapine-N-oxide (CNO) (Fig. 4c). During 4hr sessions in the circadian dark, mice chose to drink normal water or water containing CNO (see Online Methods). Relative to controls, *Crf*-BNST-hM3Dq mice consumed less CNO (Fig. 4d), whereas *Cck*-BNST-hM3Dq mice consumed more CNO (Fig. 4e). These results occurred in a concentration-dependent manner, suggesting that mice titrated their CNO intake based on subpopulation-specific hM3Dq signaling. Measures of body weight, water intake, total fluid intake, and food intake revealed no group differences (Fig. 4f-g). These findings, that *Crf*-BNST-Gq signaling is aversive and *Cck*-BNST-Gq signaling is rewarding, strengthen the conclusions from optogenetic RTPT studies (Fig. 3d-e), supporting the premise that *Crf* and *Cck* neurons drive opposing emotional states. We also identified changes in “anxiety-like” behaviors following chemogenetic and optogenetic stimulation of *Crf* and *Cck* neurons (Fig. S5), replicating previous *Crf* and *Vgat* BNST findings[36,39].

Inhibition of *Crf* and *Cck* BNST neurons during behavioral approach

Given the different states induced by DREADD modulation, we hypothesized that *Crf* and *Cck* are differentially essential for responding to appetitive salient stimuli. To test this, we analyzed male mice for behavioral approach toward female mouse urine following BNST silencing. For temporary chemogenetic inhibition, we used the inhibitory DREADD hM4Di (Fig. 4h). Slice electrophysiological recordings validated CNO-evoked decreased membrane potential (Fig. 4i). For chronic physiological inhibition, we used viral over-expression of the inwardly-rectifying potassium channel Kir2.1. Kir2.1 introduces a leak current, decreasing input resistance[40]. We observed robust spiking inhibition in Kir2.1-infected neurons relative to control neurons (Fig. 4j). Compared to control trials, male mice displayed significant behavioral preference for appetitive odorant stimuli following saline injection. However, following CNO injection, hM4Di inhibition of *Cck,* but not *Crf,* neurons diminished the preference for female mouse urine (Fig. 4k, 4m). These results indicate that *Cck*-BNST activity is essential for adaptive behavioral approach. Kir2.1 inhibition of *Cck,* but not *Crf,* neurons also reduced preference for female mouse urine (Fig 4l, 4n), further indicating the specific requirement of *Cck*-BNST activity for adaptive approach.

Crf and *Cck*: projection-specific BNST→LH functionality

We next characterized the efferent outputs of BNST neurons, observing that both *Crf* and *Cck* project strongly to the LH, MeA, and several areas throughout hypothalamus and midbrain (Fig. 5a). To assess the functionality of genetically-defined BNST→LH pathways, we asked whether photostimulation of *Crf* and *Cck* axons in the LH could reproduce the emotional states associated with BNST cell body stimulations. We expressed ChR2-eYFP (or eYFP-only) in BNST of *Crf* and *Cck* mice, and implanted fiberoptics over the LH. BNST→LH RTPT photostimulation revealed avoidance in *Crf*-BNST→LH-ChR2 mice, and preference in *Cck*-BNST→LH-ChR2 mice (Fig. 5b-c), demonstrating that genetically-defined BNST→LH pathways generate opposing emotional states.

To identify the physiological nature of distinct BNST→LH pathways, we determined the precise relationships between *Crf* or *Cck* BNST activity and *Hcrt*-LH activity. Based on divergent abundance of lateral vs. medial BNST→LH connections identified by rabies tracing, we hypothesized that BNST subpopulations are differentially connected to Hcrt and other LH cells. We crossed *Crf*-Cre and *Cck*-Cre mice with the Hcrt-eGFP reporter mouse line, expressed ChR2-mCherry in the BNST (Fig. 5d), and used *ex vivo* slice physiology to characterize BNST→LH connectivity. Importantly, we identified ChR2-mCherry BNST axons innervating the Hcrt-eGFP LH field in both *Crf* and *Cck* mice (Fig. S6). Consistent with results from input mapping, slice experiments found that 6/10 Hcrt-eGFP+ neurons received direct synaptic input from *Crf*-BNST neurons, while only 1/8 Hcrt-eGFP+ neurons received direct synaptic input from *Cck*-BNST neurons (Fig. 5e-f). In contrast to Hcrt-eGFP + connectivity differences, both *Crf* and *Cck* neurons were directly connected to ~75% of non-Hcrt-eGFP+ neurons. We observed no differences in amplitude, latency, or current decay in Hcrt-eGFP+ vs. non-Hcrt-eGFP+ cells receiving *Crf* or *Cck* input (Fig. 5g-h). These data support our overall conclusion that lateral vs. medial BNST activities are differentially linked to activities of *Hcrt* and other LH subtypes.

DISCUSSION

Limbic neural circuits critically drive and regulate emotional behavior, which is strongly implicated in psychiatric conditions of traumatic stress, compulsive reward-seeking, and dysregulated sleep-wake patterns. Here, we used genetically-encoded and pathway-specific tools to monitor, manipulate, and map discrete neural circuits, defining functional roles for previously-unrecognized pathways that coordinate behavioral responses to emotionally-salient stimuli.

Our initial studies aimed to understand how *Hcrt*-LH activity changed in response to stimuli, and how *Hcrt*-LH photostimulation generated hedonic valence-associated behavior. These questions pertain to the role of Hcrt-LH neurons in emotional arousal. For example, loss of Hcrt-LH neurons is associated with narcolepsy (sleep-like episodes that interrupt wakefulness)[41], and powerful emotional stimuli can trigger cataplectic attacks (sudden loss of muscle tone) in narcoleptic patients. These findings highlight a wide-ranging role for Hcrt in behavioral responding to salient stimuli and changing environmental conditions, with broad relevance to motivated wakefulness[42]. Yet, Hcrt peptides remain commonly known as "orexins," a term intended to ascribe appetite-stimulating properties to this system. Consequently, these ideas led to abundant reports of appetitive behaviors and reward-linked states associated with Hcrt-LH activation. Challenging this view, genetic ablation of "orexin-LH" neurons increased (rather than decreased) food intake, and orexin-LH neurons showed decreased (rather than increased) Ca^{2+} activity during feeding[43]. In the present studies, we found that *Hcrt*-LH Ca^{2+} activity was elevated in response to negative emotionally-valenced stimuli, and that *Hcrt*-LH photostimulation generated behavioral avoidance. Thus, our data do not support the hypothesis that Hcrt-LH activation is associated with a positive hedonic state. However, it remains possible that reward-linked and feeding-related aspects of the Hcrt-LH system are encoded in a pathway-specific manner, perhaps via VTA projections[44].

We compared our *Hcrt*-LH findings to *LepRb*-LH neurons, which regulate *Hcrt*-LH activity via GABAergic inhibition. Relative to *Hcrt*-LH, *LepRb*-LH neurons showed decreased activity in response to salient stimuli, and *LepRb*-LH photostimulation generated preference. While we interpret these findings within the context of their inhibitory actions onto *Hcrt*-LH neurons[27], we acknowledge that *LepRb*-LH projections to the midbrain also control related behaviors[45]. When considering that *Hcrt* and *LepRb* mark subsets of larger glutamatergic and GABAergic populations, our findings are consistent with previous reports of these broader LH cell types generating avoidance and approach[1,2]. We next compared inputs onto *Hcrt* and *LepRb* neurons, finding differences in PVN and VTA input abundance, hinting at potential functional relevance of these connections to be pursued in future studies. Despite these differences, we found abundant BNST input onto both LH cell types, highlighting a conserved organization of extended amygdala networks synapsing in LH. We used these tracing data as rationale for pursuing dissection of heterogeneous BNST→LH circuits.

One hypothesis for BNST control of emotional behavior proposed that VTA-projecting ventral BNST neurons could be functionally distinguished by classical neurotransmission mode (GABAergic vs. glutamatergic)[20]. However, GABAergic neurons comprise the majority of BNST neurons, suggesting further levels of heterogeneity. A second hypothesis

proposed that adBNST neurons could be functionally distinguished based on their axonal targets[18]. However, more than ten different neuropeptides are generated within partially-overlapping adBNST subpopulations[19,46,47], suggesting that even pathway-specific adBNST neurons encompass a diverse cellular array. A third hypothesis distinguished BNST neurons based on interneuron vs. projection neuron properties, but disregarded non-interneurons projecting elsewhere than LH or VTA[21]. We explored a fourth hypothesis by proposing that diverse functions of BNST neurons may be primarily determined based on neuropeptide-defined genetic subpopulations, rather than by classical neurotransmission mode, output target, or interneuron connectivity *per se*.

Our analyses established that connectivity of BNST neurons onto *Hcrt* vs. *LepRb* neurons corresponded to a lateral vs. medial gradient. Therefore, we identified laterally-enriched and medially-restricted BNST markers, and provided the first evidence that *Hcrt*-LH neurons receive abundant innervation from CRF-BNST neurons, but sparse innervation from CCK-BNST neurons. Prior data from our group showed that Hcrt-LH neurons are activated by stress and CRF[17], so these findings are important in identifying adlBNST and plBNST as major sources of *Hcrt*-LH CRF input.

Fiber photometry experiments found that *Crf* and *Cck* neurons are differentially activated by aversive and rewarding stimuli (Fig. 3a-c), and optogenetic experiments found that *Crf* and *Cck* are individually sufficient to generate distinct behaviors linked to opposing emotional states (Fig. 3d-e). Further, we used projection-specific photostimulation to establish that distinct BNST→LH pathways exert opposing effects on emotional behaviors (Fig. 5b-c). In considering that *Crf*-BNST→LH and *Cck*-BNST→LH mark distinct subsets of the larger overall *Vgat*-BNST→LH pathway, our findings are important in suggesting that ratios of neuropeptide modulation, rather than excitatory/inhibitory balance of fast neurotransmission, may be sufficient to explain diverse BNST behavioral effects.

BNST afferent input mapping identified differences that are likely relevant for interpreting the capabilities of these parallel circuits (Fig. 3i-j). For example, the abundance of PVN inputs onto *Crf* vs. *Cck* neurons is an intriguing candidate for an upstream mechanism explaining the divergent Ca^{2+} responses of *Crf* and *Cck* cells to salient stimuli. Following this idea, we established *Crf*-PVN neurons as an additional node in this aversion circuitry (Fig. S4g-h). We speculate that the divergent MeA input onto *Cck* vs. *Crf* neurons is functionally relevant for MeA-dependent prosocial, sexual, and aggressive behaviors[48–50].

We developed a novel model of chemogenetic self-stimulation by implementing voluntary CNO consumption for detecting cell type-specific hedonic reactivity. This approach facilitated homecage data collection in mice that might otherwise be sensitive to forced drug administration or unfamiliar environments. Our findings, in which hM3Dq-expressing mice displayed subpopulation-specific patterns of CNO intake, provide additional evidence supporting conclusions from optogenetic studies on the hedonic valence associated with *Crf* vs. *Cck* activation.

We also used experimenter-administered CNO for chemogenetic modulation, and detected “anxiety-like” behavioral changes (Fig. S5). Supporting these results, photostimulation of

Crf and *Cck* BNST neurons heightened "anxiety-like" behavior as well (Fig. S5). Thus, while either hM3Dq or ChR2 activation of either *Crf* or *Cck* neurons increased "anxiety-like" behavior, we suggest that these changes reflect generally heightened arousal states, rather than pure anxiety *per se*. We suggest that increased "anxiety-like" behavior as measured in these standard paradigms can reflect either an aversive state (avoidance of a stressful environment), or a rewarding state (a positively-reinforcing adaptive mechanism promoting safety). We posit that standard "anxiety-like" behaviors exist along the spectrum of negative and positive valence, and that these states can be modulated by activity within BNST subpopulations.

We next inhibited BNST neurons, observing that subpopulations are differentially essential for appetitive behavioral approach. In these studies of male mice, we used an ethologically-relevant odorant stimulus: urine from mice of the opposite sex[37]. As reflected in the behavior of viral controls (Fig. 4k-n), this stimulus generated significant place preference, even in sexually-naïve mice. We found that inhibition of *Cck*, but not *Crf*, neurons blocked this preference, highlighting the specific necessity of *Cck* cells for this adaptive behavior.

In the final experiments, we used a combinatorial strategy to record from LH neurons while stimulating axons from genetically-defined LH-projecting BNST neuronal subpopulations. Due to the GABAergic nature of *Crf* and *Cck* neurons, we used picrotoxin-sensitive inhibitory postsynaptic currents (IPSCs) to measure BNST→LH connectivity. Synaptic physiology data supported rabies mapping studies that identified CRF vs. CCK differences in Hcrt-LH connectivity (Fig. 5e-h). In particular, we found that 60% of Hcrt-LH neurons received direct input from *Crf*-BNST neurons, whereas only 12.5% of Hcrt-LH neurons received direct input from *Cck*-BNST neurons. In contrast, both *Crf* and *Cck* BNST neurons were directly connected to the majority of non-Hcrt LH neurons (though these exact proportions may differ with increased numbers of recordings). One remaining question is concerned with excitatory neuropeptide signaling from *Crf* vs. *Cck* neurons onto LH neurons. We hypothesize that, although we identified greater *Crf*→*Hcrt* connectivity based on GABAergic transmission, multiple physiological signals are likely conveyed in these synapses. Differential ratios of GABA/neuropeptide release onto LH neurons may be sufficient to coordinate the behavioral distinctions between *Crf*→Hcrt and *Cck*→non-Hcrt circuits. Indeed, the complex BNST→LH circuit architecture provides myriad potential mechanisms for excitation of *Hcrt*-LH neurons by *Crf*-BNST neurons, either directly by neuropeptide signaling, or indirectly by disinhibition via GABAergic LH interneurons (e.g., *LepRb*-LH neurons).

In summary, we provide the first functional characterization of two distinct neuropeptide-defined GABAergic BNST subpopulations. These findings suggest that LH-mediated behavior can be delicately controlled via balance of input from neuropeptide-defined BNST cells, rather than simply via excitatory/inhibitory neurotransmission or axonal targeting. Indeed, the mixed neurochemical phenotypes of BNST neurons allow for combinatorial modes of modulation and transmission, likely to enable large-scale multisynaptic network communication for generating the complex behaviors required for survival. Altogether, our findings provide a mechanistic framework for BNST→LH circuit dysregulations in

psychiatric disorders, and future studies will inform development of improved therapeutic approaches.

ONLINE METHODS

Animals

We used adult (8–16 week-old) male mice (*Mus musculus*) housed in plexiglass chambers at constant temperature (22 ± 1 °C) and humidity (40–60%), under a reverse circadian light-dark cycle (lights-off at 9:00 am, lights-on at 9:00 pm). Food and water were available *ad libitum*. All experiments were performed in accordance with the guidelines described in the US National Institutes of Health Guide for the Care and Use of Laboratory Animals, and approved by Stanford University Administrative Panel on Laboratory Animal Care.

Generation of *Hcrt*-IRES-Cre knock-in mice was outsourced to Cyagen Biosciences. Bacterial artificial chromosome clones containing the preprohypocretin (*Hcrt*) gene were used to target a cassette containing the internal ribosomal entry sequence (IRES) linked to Cre recombinase and a Frt-flanked Neomycin resistance gene immediately downstream of the exon2 stop codon (Fig. S1a). The target construct was electroporated into C57BL/6 embryonic stem cells, targeted clones were injected into blastocysts, resultant chimeras were bred for germline transmission, and then crossed with Flp-deletion mice to remove the Neomycin selection gene (Fig. S1b). Two out of ten pups (1 male, 1 female) were identified by positive PCR screening and used as founders of the Hcrt-IRES-Cre mouse line. Previously-generated additional Cre driver lines were also used (see below). Heterozygous male and female Cre-expressing mice were continuously backcrossed to C57BL/6J wild-type mice from the Jackson Laboratory (JAX-West; Sacramento, CA). For all data collection, we used male mice, aged 7–12 weeks at the start of experiments.

We used the following mouse lines: mHcrt-IRES-Cre (*Hcrt*; Stanford_006_mHcrt_1B1), LeprI-IRES-Cre (*LebRb*; M.G. Myers), B6(Cg)-Crh$^{tm1(cre)Zjh}$/J (*Crf*; JAX #012704), Cck$^{tm1.1(cre)Zjh}$/J (*Cck*; JAX #012706), Slc32a1$^{tm2(cre)Lowl}$/J (*Vgat*; JAX #016962), Slc17a6$^{tm2(cre)Lowl}$/J (*Vglut2*; JAX #016963), B6.Cg-*Gt(ROSA)26Sor*$^{tm9(CAG-tdTomato)Hze}$/J (*Ai14*; JAX #007909), B6;129S-*Pdyn*$^{tm1.1(cre)Mjkr}$/LowlJ (*Pdyn*; JAX #027958), B6;129S-*Tac1*$^{tm1.1(cre)Hze}$/J (*Tac1*; JAX #021877), B6.FVB(Cg)-Tg(Drd1-cre) (*Drd1*; Gensat #EY262), Tg(Six3-cre)69Frty/GcoJ (*Six3*; JAX #019755), Hcrt-eGFP reporter (A.N. van den Pol).

Surgery

Mice underwent stereotaxic surgery for fiberoptic implantation and/or viral injection, similar to previously described[26]. Mice were anesthetized with ketamine and xylazine (100 and 10 mg/kg, intraperitoneal; i.p.) and placed on a stereotaxic frame (David Kopf Instruments, Tajunga, CA). To selectively express viral constructs, we infused virus through a stainless steel 28 gauge internal microinjector (Plastics One, Inc., Roanoke, VA) connected to a 10 μl Hamilton syringe. After infusion, injector was kept in place for 5 min and then slowly withdrawn over 5 min. For optogenetic and fiber photometry and rabies mapping experiments, viral injections were unilateral. For DREADD and Kir2.1 and slice physiology

connectivity experiments, viral injections were bilateral. For optogenetic and fiber photometry experiments, mice also received unilateral fiberoptic cannula implantation, secured to the skull with MetaBond and dental cement. Fiberoptic cannulae were 200 μm for optogenetic experiments and 400 μm for fiber photometry experiments (0.48 NA; Doric Lenses). We used the following stereotactic coordinates: LH (−1.50 A/P, ±0.95 M/L, −5.10 D/V for virus, −4.90 D/V for fiberoptic), BNST (+0.10 A/P, ±0.88 M/L, −4.20 D/V for virus, −4.00 D/V for fiberoptic), PVN (−0.57 A/P, ±0.20 M/L, −5.30 D/V for virus, −5.10 D/V for fiberoptic), and lateral ventricles (−0.65 A/P, ±0.95 M/L, −2.55 D/V).

Virus Preparation

Adeno-associated viruses (AAVs) carrying Cre-inducible (double inverse orientation; DIO) transgenes were purchased from the Gene Vector and Virus Core at Stanford University (AAVs for fiber photometry, optogenetics, retrograde tracing, and Kir2.1 studies) or University of North Carolina-Chapel Hill Vector Core (AAVs for DREADD studies). Glycoprotein-deleted rabies virus for retrograde tracing (SAD ΔG EnvA-GFP, "RV*dG*-GFP"; 5×10^{10} pp/ml) was purchased from Salk Institute Gene Transfer Targeting and Therapeutics Core. We used the following AAVs: AAV-DJ-EF1α-DIO-GCaMP6f (1.1×10^{13}, 0.25 μl per hemisphere**), AAV-**DJ-EF1α-DIO-GCaMP6s (1.5×10^{13}, 0.25 **μl** per hemisphere), **AAV-**DJ-EF1α-DIO-ChR2-eYFP (1.9×10^{13}, 0.25 μl per hemisphere**),** AAV-DJ-EF1α-DIO-eYFP (1.5×10^{13}, 0.25 μl per hemisphere**),** AAV8-CAG-DIO-RG (5.0×10^{13}, 0.30 μl per hemisphere**), AAV5-**EF1α-DIO-TVA-mCherry (2.5×10^{12}, 0.30 μl per hemisphere), **AAV5-**EF1α-DIO-hM3Dq-mCherry (3.4×10^{12}, 0.50 **μl per** hemisphere), AAV5-EF1α-DIO-hM4Di-mCherry (4.0×10^{12}, 0.50 μl per hemisphere**), AAV5-**EF1α-DIO-mCherry (4.0×10^{12}, 0.50 μl per hemisphere**), AAVDJ-**CMV-DIO-Kir2.1-GFP (9.0×10^{12}, 0.25 μl per hemisphere**), AAVDJ-**CMV-DIO-GFP (6.2×10^{12}, 0.25 μl per hemisphere**), AAV-**DJ-EF1α-DIO-ChR2-mCherry (1.5×10^{14}, 0.25 **μl per** hemisphere).

General Procedures

Following recovery from fiberoptic implantation and/or viral injection (7–10 days), mice were habituated to fiberoptic patch cables (for fiber photometry and optogenetic experiments), moving freely with the tether in their homecages for an additional 7–10 days before data collection. For all behavioral studies, mice were habituated to experimenter handling in the days and weeks prior to testing. For all pharmacological and chemogenetic studies, mice were fully habituated to intraperitoneal (i.p.) saline control injections in the days and weeks prior to testing. All *in vivo* data were collected from mice under dim red light conditions, during the circadian dark (active) phase, between Zeitgeiber Time (ZT)14 and ZT22.

Fiber Photometry

Fiber photometry recordings were performed similar to as previously described[26]. Briefly, we sinusoidally modulated blue light from a 470-nm excitation LED (M470F3, Thorlabs, NJ, USA) at 211 Hz, using a custom Matlab program (MathWorks, Natick, MA, USA) and a multifunction data acquisition device (NI USB-6259, National Instruments, Austin, TX, USA). The blue light was passed through a GFP excitation filter (MF469–35, Thorlabs),

reflected off a dichroic mirror (MD498, Thorlabs), and coupled using a fiber collimation package (F240FC-A, Thorlabs) into a low-fluorescence patch cord (2m, 0.48 NA; Doric Lenses) connected to the fiberoptic implant by a zirconia sleeve (Doric Lenses). GCaMP6 fluorescence was collected through the excitation patch cord, passed through a GFP emission filter (MF525–39, Thorlabs), and focused onto a photodetector (Model 2151, Newport, Irvine, CA, USA) using a lens (LA1540-A, Thorlabs). The signal was sent to a lock- in amplifier (30-ms time constant, Model SR830, Stanford Research Systems, Sunnyvale, CA, USA) that was synchronized to 211 Hz. Signals from the amplifiers were collected at 1 KHz using a custom Matlab program and a multifunction data acquisition device (National Instruments). The photometry signal F was converted to ΔF/F by subtracting the median F from F, and dividing by the median F, when the median F is defined as the median F for the 60s baseline period preceding each 60s stimuli presentation trial.

Fiber Photometry Stimuli Presentation

To begin fiber photometry recording sessions following 7–10 days of habituation, we connected patch cords of mice to the experimental setup, and recorded Ca^{2+} activity for 120s trials. We recorded 60s of baseline Ca^{2+} activity before gently placing salient odorant (or no-scent control) stimuli into mouse homecages. Salient odorant stimuli were provided on small 1cm x 1cm pieces of cotton (Nestlet). Stimuli included no-scent control (200 μl saline), female or male mouse scent (200 μl of female or male mouse urine), or predator scent (5 μl TMT; fox urine scent). Mouse urine was collected from same-sex group-housed adult (8–12 week-old) mice from several different cages in a different area of the facility from the experimental room, stored in tubes containing pooled samples from several male or female mice, and used for testing within 1hour of collection.

Photostimulation and Real-Time Place Testing (RTPT)

All *in vivo* optogenetic stimuli (10ms pulses, at 5Hz or 10Hz) were generated by a waveform generator (Master-8; AMPI, Jerusalem, Israel) that triggered blue-light lasers (473 nm; LaserGlow). Laser power was adjusted such that the light exiting the fiber optic cable was 8–16 mW. Behavior was recorded by overhead video camera, and scored offline by experimenters blinded to the experimental group or stimulation parameter. Subjects were placed into the “no-stimulation” side of a two-chambered 52 × 26 cm apparatus filled with fresh bedding, and upon crossing to the opposite “stimulation” side, received stimulation (473nm; 5Hz, 10Hz, or no light) until returning to the no-stimulation side, upon which stimulation ceased. The 10 min sessions began when the subject first fully crossed (all four paws) from the no-stimulation side to the stimulation-paired side.

No-stimulation control trials showed that the behavioral apparatus was unbiased (n=94 mice; 50.71 ± 0.49 % time spent on the “stimulation-paired” side). In addition to the unbiased apparatus, we also used an unbiased paradigm, in which the stimulation-paired side was fully counterbalanced across testing. Mice underwent repeated RTPT tests with different stimulation parameters that were separated from each other by 5–10 days, and counterbalanced on the order of stimulation parameter tested (no light, 5Hz, or 10Hz). All trials were balanced such that equal numbers of mice from each group, for each stimulation

parameter trial, received stimulation frequencies on a given side of the apparatus. Furthermore, we counterbalanced the stimulation-paired side for each individual, such that half of mice from each group received stimulation on the same side as the previous test, and half of the mice from each group received stimulation on the opposite side from the previous test.

Drugs

Double Hcrt-R antagonist MK6096 (filorexant[28]) was dissolved in 50% saline/50% PEG-400 at a concentration of 2.0 mg/ml and administered i.p. at a dose of 5.0 mg/kg 30mins prior to behavioral testing. Norbinaltorphimine (norBNI) was dissolved in saline at a concentration of 1.0 mg/ml and administered i.p. at a dose of 10.0 mg/kg 24hrs prior to behavioral testing. Designer receptor ligand clozapine-N-oxide (CNO) was dissolved in 100% saline at a concentration of 0.20 mg/ml and administered i.p. at a dose of 2 mg/kg 30 minutes prior to behavioral testing. For self-stimulation studies, CNO was dissolved in tap water at concentrations of 25 mg/l, 50 mg/l, or 100 mg/l (described below).

Monosynaptic Modified-Rabies Viral Tracing

Three weeks following unilateral viral infusion of AAV5-DIO-TVA-mCherry and AAV8-DIO-RG into either the LH or the BNST (1:1 viral mixture, 0.6 μl total volume), 0.5 μl of the RV*dG*-GFP modified rabies was injected into the same site. Five days later, mice received bilateral colchicine infusions into the lateral ventricles (1.0 μl of 7 μg/ml solution per hemisphere, for neuropeptide immunostaining). Following colchicine infusions (24–48h later), mice were anesthetized and perfused, and brains were dissected and processed as described below. Starter cells were identified as neurons co-expressing TVA-mCherry and RV*dG*-GFP in the injection site. Input cells were defined as all RV*dG*-GFP-labeled cells that were not starter cells. For all brains with identified starter cells (n=15 mice), we imaged coronal sections (120 μm intervals; every fourth consecutive slice), from the rostral prefrontal cortex to the caudal brainstem. We counted the number of input cells, and categorized them into brain subregions based on cytoarchitectural DAPI-assisted analysis, according to major delineations made by the Allen Institute and Paxinos & Watson mouse brain atlases. After generating the total sum of all input cells from each brain, we converted the number of input cells from each region into the percentage of total input cells for each brain.

CNO-hM3Dq DREADD Self-Stimulation

In rodents, oral or systemic CNO administration led to peak concentrations in brain and plasma within 5–15 minutes[51,52]. The rapid pharmacokinetic absorption and distribution properties of CNO, together with the favorable water solubility profile of commercial CNO, made this drug suitable for establishing a model of voluntary oral consumption (analogous to established two-bottle choice limited-access drinking paradigms for ethanol and sucrose consumption[53,54]). Thus, under properly controlled settings, voluntary CNO consumption can be used for studying cell type-specific chemogenetic self-stimulation of neuronal hM3Dq DREADD signaling. We performed these experiments during the maximal rate of circadian fluid consumption, in which adult male C57BL/6J mice typically consume 1–2 ml

of regular water (30–50% of their total daily fluid consumption) in a 4h period (ZT14 – ZT18).

We designed CNO concentrations based on the range of behaviorally-active doses of i.p. CNO administered. For example, we selected CNO concentrations such that a 25g mouse consuming 1ml of the solution would lead to systemic CNO doses of 1.0 – 4.0 mg/kg (ex: 1ml * 50 mg/l * 0.025kg = 2 mg/kg). Because 2 mg/kg i.p. CNO led to behavioral effects lasting on the order of 1–2h in separate studies, we reasoned that equivalent doses of orally consumed CNO over a 4h drinking session would be representative of the chemogenetic effects produced by i.p. CNO injection. Control virus-injected mice showed no significant aversion or preference for the taste of CNO at concentrations 25–100 mg/l (Fig. 4c-d). Thus, any significant differences in CNO intake and preference observed between DREADD-expressing and viral control mice were attributable to Cre-specific chemogenetic CNO-DREADD effects rather than simply differences in taste reactivity. Furthermore, we fully counterbalanced the side of the CNO-containing water bottle across groups, and switched the side of the CNO-containing bottle every other day in order to minimize the potential of an inherent cage side bias, as well as to minimize the potential development of conditioned avoidance of (or preference for) the side associated with the CNO bottle.

During recovery from surgery (BNST-AAV5-DIO-hM3Dq or BNST-AAV5-DIO-mCherry), *Crf and Cck* mice received 10–14 days of acclimation to single-housing and drinking tap water from two 10 ml plastic pipette tubes with metal sipper spouts, placed on either side of the cage. Baseline measurements of body weight, water consumption, and food consumption did not significantly differ between groups. The experiment consisted of three phases, with each phase consisting of four consecutive days of 4-hour CNO drinking sessions. Each progressive phase included a new concentration of CNO (25, 50, and 100 mg/liter, in escalating order), with three days of water-only drinking in between each phase (to minimize potential pharmacokinetic and pharmacodynamic CNO tolerance). CNO solutions were protected from light to prevent degradation, and fresh CNO solutions were provided every other day. Each day, we recorded body and food weights. During food weighing, cage floor was checked for pieces of food that fell through the cage top (<0.1% of all data points collected). Next, one of the two water tubes was replaced with a tube of CNO-water, and fluid volumes were recorded to the nearest 0.1 ml. Four hours later, fluid volumes and food weights were recorded again; the CNO tube was removed, and replaced with the original regular water tube.

Primary variables included: CNO intake (mg/kg), CNO preference ratio (volume of CNO-water consumed/volume of total fluid consumed), total fluid intake (ml of CNO-water + normal water consumed), and food intake (g/kg), as previously described[53,54]. We incorporated analyses of multiple consummatory-related variables in order to dissociate motivation for CNO's cell type-specific chemogenetic properties vs. generalized taste- or thirst-driven factors (Fig. 4f-g).

Behavioral Approach Testing

In ten-minute sessions, we videorecorded mice after being placed in the center of a two-chambered apparatus (52cm x 26cm), with each side containing an inverted wire mesh

cylinder, and each cylinder containing either no-scent control odorant stimuli, or female mouse odorant stimuli (physically inaccessible). For hM4Di DREADD inhibition studies, the order of saline and CNO sessions was counterbalanced, and each test was separated by 5–10 days. For chronic inhibition studies, Kir2.1 and GFP control mice first underwent control test sessions (control stimuli on both ends), followed 5–10 days later by experimental test sessions (control stimuli on one end vs. female mouse odorant stimuli on the other end). In all trials, we quantified the time spent on the test stimulus-paired side.

Anxiety-Like Behavior Testing

Mice were videorecorded for 5 min immediately after being placed in the center of the open field test (OFT) or elevated plus maze (EPM). For DREADD studies, mice underwent the OFT and EPM 30 minutes following i.p. injection of either saline or CNO. For optogenetic studies, mice were tested immediately following either homecage no-light control stimulation, or photostimulation (1-second train of 10Hz stimulation, every 30 seconds, for 5 mins). The OFT consisted of a 44cm x 44cm white acrylic square box, with the center defined as the inner 22cm x 22cm square. The EPM consisted of a black acrylic apparatus elevated 30cm off the floor, consisting of two symmetrical open arms, and two symmetrical closed arms (each arm 5cm x 16cm), with a 5cm x 5cm square connecting the four arms in the center. We quantified OFT videos for distance traveled and center time. Distance traveled was converted to mean velocity (cm/s) for data analysis and presentation. We manually scored EPM videos for the number of closed and open arm entries, and the time spent in the open arms (defining an open arm entry and open arm time as when mice had at least their two front paws into the open arm).

Electrophysiology.

Coronal hypothalamic slices containing the BNST or LH (250 mm) were prepared from 3–4.5-month-old mice, at least 4 weeks following virus injection. Mice were deeply anesthetized with isoflurane before being transcardially perfused with an ice-cold, artificial cerebrospinal fluid (CSF), consisting of: 124 mM NaCl, 4 mM KCl, 26 mM NaHCO3, 1 mM Na2PO4, 10 mM glucose, 2 mM CaCl2 and 1.2 mM MgSO4, saturated with 95% O2/ 5% CO2. Slices were cut on microslicer (DTK-1000, Ted Pella) in ice-cold high-sucrose cutting solution consisting of: 254mM Sucrose, 1.25 mM NaH2PO4, 24 mM NaHCO3, 3 mM KCl, 2 mM CaCl2, 2 mM MgCl2, and 10 mM glucose, saturated with 95% O2/5% CO2, prior to slicing. Slices were then placed in a recovery chamber containing artificial cerebrospinal fluid (CSF), saturated with 95% O2/ 5% CO2 and allowed to recover for 1hr prior to recording @ 32° C. Whole-cell patch-clamp recordings from eYFP+, mCherry+, or eGFP+ neurons were carried out using thin-walled borosilicate glass pipettes (Warner Instruments) with pipette resistance values of 3–5 MOhms. All recordings were carried out at room temperature (RT; 21–22 C). For whole-cell current-clamp recordings of identified neurons, pipettes were filled with an internal solution consisting of: 115 mM potassium gluconate, 20 mM KCl, 1.5mM MgCl2, 10 mM Phosphocreatine - Tris, 10 mM HEPES, 0.1 mM EGTA, 2 mM Mg-ATP and 0.5 mM Na-GTP (pH 7.3). For validation of hM3Dq and hM4Di, CNO (10 μM) was bath applied while the cell was at RMP. Changes in RMP were measured 3min post application. For Kir2.1 validation, cells were kept at ~−60mV, while a series of current steps were applied. For whole cell voltage-clamp recordings from identified

Hcrt-eGFP+ and Hcrt-eGFP- neurons, pipettes were filled with a high-Cl internal solution consisting of: 135 mM CsCl, 10 mM HEPES, 10 mM EGTA, 2 mM NaCl, 4 mM Mg-ATP, 5 mM TEA-Cl, 1 mM QX-314-Cl and 0.1 mM spermine (pH 7.3). These recordings were carried out at 60 mV in the presence of NBQX (10 mM), TTX (1 μM), and 4AP (200 μM). Picrotoxin was added (100 μM) to recording aCSF to confirm the inhibitory nature of recorded currents. Series resistance (10–25 MΩ) was monitored with a 5 mV hyperpolarizing pulse (10 ms) given during every epoch, and only recordings that remained stable over the period of data collection were used. Photostimulation was carried out using a TTL-controlled ultra-high power white LED (ThorLabs), passing through an enhanced green fluorescent protein (EGFP) filter cube, through the objective with an intensity of ~5 mW. Pulse duration was 1 ms for evaluation of synaptic release. All recordings were conducted using a Multiclamp 700B amplifier (Molecular Devices) filtered at 3 kHz and digitized at 10 kHz using a Heka digitizer and were acquired and analyzed using Axograph X.

Histology, Immunostaining, Microscopy, and Image Analysis

Mice were anesthetized with ketamine and xylazine (100 and 10 mg/kg, i.p.) and transcardially perfused with 5 ml 1x phosphate buffered saline (PBS), followed by 20 ml paraformaldehyde (PFA; 4%, in PBS). Brains were rapidly extracted, postfixed overnight (12–18h) in 4% PFA at 4°C, and cryoprotected for 48–96h at 4°C in sucrose solution (30% sucrose in PBS containing 0.1% NaN3) until sunk. Brains were sliced in 30 μm coronal sections at −22°C on a cryostat (Leica Microsystems), collected consecutively in 24-well plates containing PBS with 0.1% NaN3, covered in light-protective material, and stored at 4°C until imaging and/or immunohistochemical processing. We used the following antibodies: goat anti-orexinA (Hcrt; 1:1000, Santa Cruz sc-8070), goat anti-MCH (1:1000, Santa Cruz sc-14509), chicken anti-TH (1:1000, Aves TYH), rabbit anti-CRF (1:250, Immunostar 20084, i.c.v. colchicine treatment required), rabbit anti-CCK (1:250, Immunostar 20078, i.c.v. colchicine treatment required), rabbit anti-cFos (1:1000, Immunostar 26209), donkey anti-goat Alexa 594 (1:500, Jackson ImmunoResearch Laboratories, Inc. 705–585-147), donkey anti-chicken Alexa 594 (1:500, Jackson ImmunoResearch Laboratories, Inc. 703–585-155), donkey anti-rabbit Alexa 488 (1:500, Jackson ImmunoResearch Laboratories, Inc. 711–545-152), donkey anti-rabbit Alexa 594 (1:500, Jackson ImmunoResearch Laboratories, Inc. 711–585-152), donkey anti-rabbit Alexa 647 (1:500, Jackson ImmunoResearch Laboratories, Inc., 711–607-003). Sections were washed in PBS for 5 min and then incubated for 1hr in a blocking solution of PBS with 0.3% Triton X-100 (PBST) containing 4% bovine serum albumin (BSA). Next, we incubated slices in primary antibodies overnight for 12–18h, in 4% BSA/PBST block solution. After three 5-min PBS washes, sections were again incubated in blocking solution for 1hr, and then incubated for an additional 2hr in blocking solution containing secondary antibodies. After three final 5-min PBS washes, sections were mounted onto gelatin-coated glass slides (FD Neurotechnologies, Inc.; PO101), and coverslipped with Fluoroshield containing DAPI Mounting Media (Sigma; F6057). Images were collected on a Zeiss LSM 710 confocal microscope using ZEN software, and minimally processed using Image J (NIH) to enhance brightness and contrast for optimal representation. Digital images were analyzed in parallel offline, with the experimenter blind to the group identity during quantitative analyses. Pre-established exclusion criteria included lack of accurate stereotaxic

targeting and/or viral expression, thus <3% of data points were excluded based on post-mortem brain tissue analyses.

Statistics

All data are presented as mean ± standard error of the mean (S.E.M.). No statistical methods were used to pre-determine sample sizes but our sample sizes are similar to those reported in previous publications using optogenetic and chemogenetic tools for the study of the stress and reward circuits[26,27]. Individual data points are shown for all graphs in all figures, because data distribution was assumed to be normal, but not formally tested. Mice were removed from analyses if no viral expression was found (<2% of all cases). We used one-way and two-way ANOVA (incorporating repeated measures [RM-ANOVA] where appropriate), and performed post-hoc comparisons using the Bonferroni correction. We plotted and analyzed all data using Prism 7.0 (GraphPad Software). A Life Sciences Reporting Summary is available.

Data and Code Accessibility

The data and code that support the findings of this study are available from the corresponding author upon reasonable request.

Supplementary Material

Refer to Web version on PubMed Central for supplementary material.

ACKNOWLEDGMENTS

We acknowledge all de Lecea lab members, A. D. Abraham, and P. F. Apostolides for critical feedback. We thank A. Khan, T.A. Lucas, K. Malacon, M. Silvestre, D. Hoang, C. Liang, K. Choudhury, K. Cruz, and A. Yao for excellent technical assistance. This work was supported by National Institutes of Health grants F32 AA022832 (W.J.G), R01 MH087592 (L.d.L.), R01 MH102638 (L.d.L.), and F32 MH106206 (D.J.C.). We also recognize support from Dr. Andrew Olson and the Stanford Neuroscience Microscopy Service, NIH NS069375.

REFERENCES

1. Jennings JH , Rizzi G , Stamatakis AM , Ung RL & Stuber GD The inhibitory circuit architecture of the lateral hypothalamus orchestrates feeding. Science 341, 1517–1521 (2013). [PubMed: 24072922]
2. Nieh EH , et al. Decoding neural circuits that control compulsive sucrose seeking. Cell 160, 528–541 (2015). [PubMed: 25635460]
3. de Lecea L , et al. The hypocretins: hypothalamus-specific peptides with neuroexcitatory activity. Proceedings of the National Academy of Sciences of the United States of America 95, 322–327 (1998). [PubMed: 9419374]
4. Sakurai T , et al. Orexins and orexin receptors: a family of hypothalamic neuropeptides and G protein-coupled receptors that regulate feeding behavior. Cell 92, 573–585 (1998). [PubMed: 9491897]
5. Baimel C , et al. Orexin/hypocretin role in reward: implications for opioid and other addictions. British journal of pharmacology 172, 334–348 (2015). [PubMed: 24641197]
6. Giardino WJ & de Lecea L Hypocretin (orexin) neuromodulation of stress and reward pathways. Current opinion in neurobiology 29, 103–108 (2014). [PubMed: 25050887]
7. Li SB , Giardino WJ & de Lecea L Hypocretins and Arousal. Current topics in behavioral neurosciences (2016).

8. Bourgin P , et al. Hypocretin-1 modulates rapid eye movement sleep through activation of locus coeruleus neurons. The Journal of neuroscience : the official journal of the Society for Neuroscience 20, 7760–7765 (2000). [PubMed: 11027239]
9. Peyron C , et al. Neurons containing hypocretin (orexin) project to multiple neuronal systems. The Journal of neuroscience : the official journal of the Society for Neuroscience 18, 9996–10015 (1998). [PubMed: 9822755]
10. Boutrel B , et al. Role for hypocretin in mediating stress-induced reinstatement of cocaine-seeking behavior. Proceedings of the National Academy of Sciences of the United States of America 102, 19168–19173 (2005). [PubMed: 16357203]
11. Hata T , et al. Intra-ventral tegmental area or intracerebroventricular orexin-A increases the intracranial self-stimulation threshold via activation of the corticotropin-releasing factor system in rats. The European journal of neuroscience 34, 816–826 (2011). [PubMed: 21848921]
12. Borgland SL , et al. Orexin A/hypocretin-1 selectively promotes motivation for positive reinforcers. The Journal of neuroscience : the official journal of the Society for Neuroscience 29, 11215–11225 (2009). [PubMed: 19741128]
13. Muschamp JW , et al. Hypocretin (orexin) facilitates reward by attenuating the antireward effects of its cotransmitter dynorphin in ventral tegmental area. Proceedings of the National Academy of Sciences of the United States of America 111, E1648–1655 (2014). [PubMed: 24706819]
14. Gonzalez JA , Iordanidou P , Strom M , Adamantidis A & Burdakov D Awake dynamics and brain-wide direct inputs of hypothalamic MCH and orexin networks. Nature communications 7, 11395 (2016).
15. Sakurai T , et al. Input of orexin/hypocretin neurons revealed by a genetically encoded tracer in mice. Neuron 46, 297–308 (2005). [PubMed: 15848807]
16. Tsujino N , et al. Cholecystokinin activates orexin/hypocretin neurons through the cholecystokinin A receptor. The Journal of neuroscience : the official journal of the Society for Neuroscience 25, 7459–7469 (2005). [PubMed: 16093397]
17. Winsky-Sommerer R , et al. Interaction between the corticotropin-releasing factor system and hypocretins (orexins): a novel circuit mediating stress response. The Journal of neuroscience : the official journal of the Society for Neuroscience 24, 11439–11448 (2004). [PubMed: 15601950]
18. Kim SY , et al. Diverging neural pathways assemble a behavioural state from separable features in anxiety. Nature 496, 219–223 (2013). [PubMed: 23515158]
19. Lebow MA & Chen A Overshadowed by the amygdala: the bed nucleus of the stria terminalis emerges as key to psychiatric disorders. Molecular psychiatry 21, 450–463 (2016). [PubMed: 26878891]
20. Jennings JH , et al. Distinct extended amygdala circuits for divergent motivational states. Nature 496, 224–228 (2013). [PubMed: 23515155]
21. Marcinkiewcz CA , et al. Serotonin engages an anxiety and fear-promoting circuit in the extended amygdala. Nature 537, 97–101 (2016). [PubMed: 27556938]
22. Gunaydin LA , et al. Natural neural projection dynamics underlying social behavior. Cell 157, 1535–1551 (2014). [PubMed: 24949967]
23. Zhang F , Aravanis AM , Adamantidis A , de Lecea L & Deisseroth K Circuit-breakers: optical technologies for probing neural signals and systems. Nature reviews. Neuroscience 8, 577–581 (2007). [PubMed: 17643087]
24. Armbruster BN , Li X , Pausch MH , Herlitze S & Roth BL Evolving the lock to fit the key to create a family of G protein-coupled receptors potently activated by an inert ligand. Proceedings of the National Academy of Sciences of the United States of America 104, 5163–5168 (2007). [PubMed: 17360345]
25. Wall NR , Wickersham IR , Cetin A , De La Parra M & Callaway EM Monosynaptic circuit tracing in vivo through Cre-dependent targeting and complementation of modified rabies virus. Proceedings of the National Academy of Sciences of the United States of America 107, 21848–21853 (2010). [PubMed: 21115815]
26. Eban-Rothschild A , Rothschild G , Giardino WJ , Jones JR & de Lecea L VTA dopaminergic neurons regulate ethologically relevant sleep-wake behaviors. Nature neuroscience 19, 1356–1366 (2016). [PubMed: 27595385]

27. Bonnavion P , Jackson AC , Carter ME & de Lecea L Antagonistic interplay between hypocretin and leptin in the lateral hypothalamus regulates stress responses. Nature communications 6, 6266 (2015).
28. Winrow CJ , et al. Pharmacological characterization of MK-6096 - a dual orexin receptor antagonist for insomnia. Neuropharmacology 62, 978–987 (2012). [PubMed: 22019562]
29. Li SB , Nevárez N , Giardino WJ & de Lecea L Optical Probing of Orexin/Hypocretin Receptor Antagonists. *Sleep***in press**(2018).
30. Crestani CC , et al. Mechanisms in the bed nucleus of the stria terminalis involved in control of autonomic and neuroendocrine functions: a review. Current neuropharmacology 11, 141–159 (2013). [PubMed: 23997750]
31. Ju G & Swanson LW Studies on the cellular architecture of the bed nuclei of the stria terminalis in the rat: I. Cytoarchitecture. The Journal of comparative neurology 280, 587–602 (1989). [PubMed: 2708568]
32. Krettek JE & Price JL Amygdaloid projections to subcortical structures within the basal forebrain and brainstem in the rat and cat. The Journal of comparative neurology 178, 225–254 (1978). [PubMed: 627625]
33. Radley JJ , Gosselink KL & Sawchenko PE A discrete GABAergic relay mediates medial prefrontal cortical inhibition of the neuroendocrine stress response. The Journal of neuroscience : the official journal of the Society for Neuroscience 29, 7330–7340 (2009). [PubMed: 19494154]
34. Weller KL & Smith DA Afferent connections to the bed nucleus of the stria terminalis. Brain research 232, 255–270 (1982). [PubMed: 7188024]
35. Dong HW & Swanson LW Projections from bed nuclei of the stria terminalis, posterior division: implications for cerebral hemisphere regulation of defensive and reproductive behaviors. The Journal of comparative neurology 471, 396–433 (2004). [PubMed: 15022261]
36. Pleil KE , et al. NPY signaling inhibits extended amygdala CRF neurons to suppress binge alcohol drinking. Nature neuroscience 18, 545–552 (2015). [PubMed: 25751534]
37. McHenry JA , et al. Hormonal gain control of a medial preoptic area social reward circuit. Nature neuroscience 20, 449–458 (2017). [PubMed: 28135243]
38. Fuzesi T , Daviu N , Wamsteeker Cusulin JI , Bonin RP & Bains JS Hypothalamic CRH neurons orchestrate complex behaviours after stress. Nature communications 7, 11937 (2016).
39. Mazzone CM , et al. Acute engagement of Gq-mediated signaling in the bed nucleus of the stria terminalis induces anxiety-like behavior. Molecular psychiatry (2016).
40. Lin CW , et al. Genetically increased cell-intrinsic excitability enhances neuronal integration into adult brain circuits. Neuron 65, 32–39 (2010). [PubMed: 20152111]
41. Lin L , et al. The sleep disorder canine narcolepsy is caused by a mutation in the hypocretin (orexin) receptor 2 gene. Cell 98, 365–376 (1999). [PubMed: 10458611]
42. Eban-Rothschild A , Giardino WJ & de Lecea L To sleep or not to sleep: neuronal and ecological insights. Current opinion in neurobiology 44, 132–138 (2017). [PubMed: 28500869]
43. Gonzalez JA , et al. Inhibitory Interplay between Orexin Neurons and Eating. Current biology : CB 26, 2486–2491 (2016). [PubMed: 27546579]
44. Baimel C , Lau BK , Qiao M & Borgland SL Projection-Target-Defined Effects of Orexin and Dynorphin on VTA Dopamine Neurons. Cell reports 18, 1346–1355 (2017). [PubMed: 28178514]
45. Leinninger GM , et al. Leptin acts via leptin receptor-expressing lateral hypothalamic neurons to modulate the mesolimbic dopamine system and suppress feeding. Cell metabolism 10, 89–98 (2009). [PubMed: 19656487]
46. Nguyen AQ , Dela Cruz JA , Sun Y , Holmes TC & Xu X Genetic cell targeting uncovers specific neuronal types and distinct subregions in the bed nucleus of the stria terminalis. The Journal of comparative neurology 524, 2379–2399 (2016). [PubMed: 26718312]
47. Poulin JF , Arbour D , Laforest S & Drolet G Neuroanatomical characterization of endogenous opioids in the bed nucleus of the stria terminalis. Progress in neuro-psychopharmacology & biological psychiatry 33, 1356–1365 (2009). [PubMed: 19583989]
48. McCarthy EA , et al. DREADD-induced silencing of the medial amygdala reduces the preference for male pheromones and the expression of lordosis in estrous female mice. The European journal of neuroscience 46, 2035–2046 (2017). [PubMed: 28677202]

49. Shemesh Y , et al. Ucn3 and CRF-R2 in the medial amygdala regulate complex social dynamics. Nature neuroscience 19, 1489–1496 (2016). [PubMed: 27428651]

50. Unger EK , et al. Medial amygdalar aromatase neurons regulate aggression in both sexes. Cell reports 10, 453–462 (2015). [PubMed: 25620703]

51. Bender D , Holschbach M & Stocklin G Synthesis of n.c.a. carbon-11 labelled clozapine and its major metabolite clozapine-N-oxide and comparison of their biodistribution in mice. Nuclear medicine and biology 21, 921–925 (1994). [PubMed: 9234345]

52. Guettier JM , et al. A chemical-genetic approach to study G protein regulation of beta cell function in vivo. Proceedings of the National Academy of Sciences of the United States of America 106, 19197–19202 (2009). [PubMed: 19858481]

53. Giardino WJ , et al. Control of chronic excessive alcohol drinking by genetic manipulation of the Edinger-Westphal nucleus urocortin-1 neuropeptide system. Translational psychiatry 7, e1021 (2017). [PubMed: 28140406]

54. Giardino WJ & Ryabinin AE CRF1 receptor signaling regulates food and fluid intake in the drinking-in-the-dark model of binge alcohol consumption. Alcoholism, clinical and experimental research 37, 1161–1170 (2013).

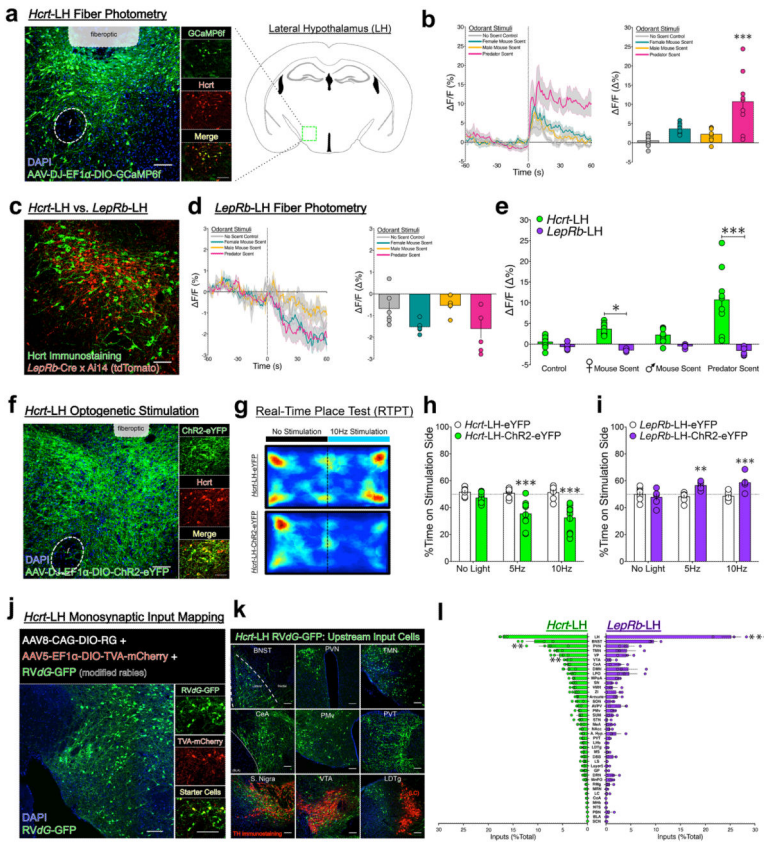

Figure 1. LH neurons: physiology, behavior, and mapping input neurocircuitry.

(a) Left, representative image of *Hcrt*-LH-AAV-DIO-GCaMP6f expression and fiberoptic placement; inset panels show specific co-expression of viral GCaMP6f labeling (green) with Hcrt immunostaining (red), replicated independently with similar results in six mice. Right, schematic of coronal brain slice showing target area in the LH. **(b)** Left; mean (± S.E.M.) fluorescent Ca^{2+} activity traces from *in vivo* fiber photometry recordings of *Hcrt*-LH neurons during baseline 60s (left of dashed line), and during 60s exposure to salient odorant stimuli (right of dashed line). Right; mean (± S.E.M.) fluorescence levels during the 60s stimuli exposure phase (n=6 mice; 1–2 trials with each stimulus per subject, one-way ANOVA; $F_{3,32} = 11.38$, $p < 0.0001$, Bonferroni post-hoc comparison ***$p < 0.0001$ vs. no-scent control). **(c)** Representative image of the LH of *LepRb*-Cre x Cre-inducible Ai14 mice (tdTomato, red), with Hcrt immunostaining (green) demonstrating complete lack of *LepRb*-Cre and Hcrt co-expression, replicated independently with similar results in four mice. **(d)** Left; mean (± S.E.M.) fluorescent Ca^{2+} activity traces from *in vivo* fiber photometry recordings of *LepRb*-LH neurons during baseline 60s (left of dashed line), and during 60s exposure to salient odorant stimuli (right of dashed line). Right; mean (± S.E.M.) fluorescence levels during the 60s stimuli exposure phase (n=4 mice; 1–2 trials with each stimulus per subject, one-way ANOVA; $F_{3,20} = 5.01$, $p = 0.0094$). **(e)** Direct comparison of mean (± S.E.M.) fluorescence levels from *Hcrt*-LH (n=6) and *LepRb*-LH (n=4) mice during the 60s stimuli exposure phase (two-way ANOVA; stimuli x LH cell type interaction $F_{3,52} = 8.75$, $p < 0.0001$, *Hcrt* vs. *LepRb* Bonferroni post-hoc comparisons *$p < 0.05$ ***$p < 0.0001$) **(f)** Representative image of *Hcrt*-LH-AAV-DIO-ChR2-eYFP expression; inset

panels show specific co-expression (yellow) of viral ChR2-eYFP labeling (green) with Hcrt immunostaining (red), replicated independently with similar results in ten mice. **(g)** Representative heat maps indicating activity of *Hcrt*-LH-eYFP and *Hcrt*-LH-ChR2-eYFP mice in the RTPT apparatus during 10Hz stimulation trial. **(h)** *Hcrt*-LH-ChR2 photostimulation is aversive in the RTPT (n=7 eYFP, n=10 ChR2-eYFP), two-way repeated measures ANOVA; ChR2 x stimulation interaction: $F_{2,30} = 6.72$, $p = 0.004$, Bonferroni post-hoc comparisons ***$p < 0.0005$ vs. *Hcrt*-LH-eYFP control group). Centre and error bars are mean ± S.E.M. **(i)** *LepRb*-LH-ChR2 photostimulation is rewarding in the RTPT (n=8 *LepRb*-LH-eYFP mice, n=6 *LepRb*-LH-ChR2-eYFP mice, two-way repeated measures ANOVA; ChR2 x stimulation interaction: $F_{2,24} = 10.18$, $p = 0.0006$, Bonferroni post-hoc comparisons **$p < 0.005$, ***$p < 0.0005$ vs. *LepRb*-LH-eYFP control group). **(j)** Representative image of *Hcrt*-LH-RV*dG*-GFP expression; inset panels show starter cells co-expressing RV*dG*-GFP (green) and AAV5-DIO-TVA-mCherry (red), replicated independently with similar results with four mice **(k)** Representative images of upstream RV*dG*-GFP cells that provide direct monosynaptic inputs on *Hcrt*-LH neurons. **(l)** Visualization of relative abundance of brainwide inputs onto *Hcrt* LH neurons vs. *LepRb* LH neurons (n=4 *Hcrt*-LH, n=3 *LepRb*-LH, two-way RM-ANOVA; LH subpopulation x input region interaction: $F_{40,205} = 4.03$, $p < 0.0001$, Bonferroni post-hoc comparisons **$p < 0.005$, ***$p < 0.0005$ vs. opposite LH subpopulation). Centre and error bars are mean ± S.E.M. Abbreviations: AH; anterior hypothalamus, AVPV; anteroventral periventricular nuclei, BLA; basolateral amygdala, BNST; bed nuclei of the stria terminalis, CeA; central nucleus of the amygdala, CoA; cortical amygdala nuclei, DBB; diagonal band of Broca; DMH; dorsomedial hypothalamus, DRN; dorsal raphe nuclei, GP; globus pallidus, Layer 5; fifth and/or sixth-layer pyramidal neurons (sparsely, in various anterior cortical regions), LC; locus coeruleus, LDTg; laterodorsal tegmentum, LH; lateral hypothalamus, LPO; lateral preoptic area, LS; lateral septum, MeA; medial amygdala, MHb; medial habenula, MnPO; median preoptic nucleus, MPoA; medial preoptic area, MRN; median raphe nucleus, MS; medial septum, NAcc; nucleus accumbens, NTS; nucleus tractus solitarus, PBN; parabrachial nucleus, PMv; ventral premammilary nucleus, PVN; paraventricular hypothalamus, PVT; paraventricular thalamus, RMg; raphe magnus, SCN; suprachiasmatic nuclei, SNc; substantia nigra compacta, SON; supraoptic hypothalamus, STN; subthalamic nucleus, SUM; supramammilary nucleus, TMN; tuberomammilary nucleus, VMH; ventromedial hypothalamus, VP; ventral pallidum, VTA; ventral tegmental area, ZI; zona incerta. Scalebars: all 100 μm.

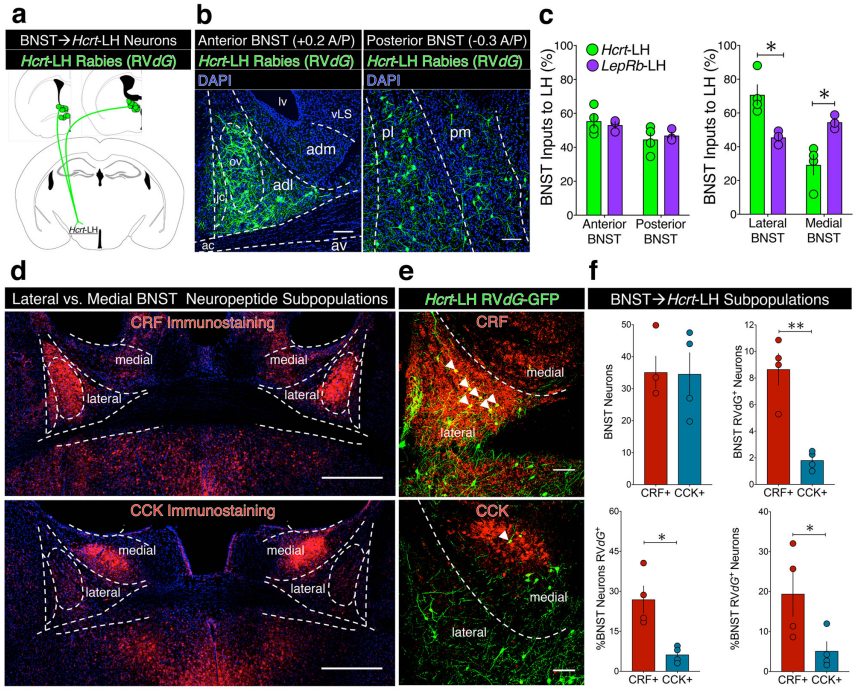

Figure 2. Neurochemical identification of genetically-defined BNST→LH circuitry

(a) Schematic showing upstream RV*dG*-GFP BNST cells that directly synapse onto downstream *Hcrt*-LH cells. **(b)** Representative images of DAPI-labeled coronal anterior (left) and posterior (right) BNST slices overlaid with subnuclei distinctions and anatomical landmarks, showing preferential expression of *Hcrt*-LH-RVdG-GFP input cells in lateral vs. medial BNST neurons, replicated independently with similar results in four mice. **(c)** Quantification of BNST→LH input cells (n=4 *Hcrt*-LH, n=3 *LepRb*-LH mice; two-way ANOVA; LH subpopulation x BNST division interaction for Anterior vs. Posterior: $F_{1,10}$ = 0.43, p = 0.53 n.s.; LH subpopulation x BNST division interaction for Lateral vs. Medial: $F_{1,10}$ = 23.50, p = 0.0007, Bonferroni post-hoc comparisons *p = 0.0129 vs. opposite LH subpopulation). Centre and error bars are mean ± S.E.M. **(d)** Representative images of CRF (top) and CCK (bottom) neuropeptide immunostaining (red) in coronal BNST slices. **(e)** Representative images of *Hcrt*-LH-RV*dG*-GFP dorsal BNST stained for CRF (top) and CCK (bottom). White arrowheads indicate double-labeled cells. Note the abundance of Hcrt-LH-RV*dG*-GFP BNST input cells co-expressing CRF, but not CCK. **(f)** Top left: equal numbers of CRF and CCK neuropeptide neurons (mean per hemisphere, per slice, n=4 mice, two-tailed paired t-test; t_3 = 0.09, p = 0.93). Top right: significantly greater number *Hcrt*-LH-RVdG-GFP+ neurons co-expressing CRF vs. CCK (mean per slice, per hemisphere, n=4 mice, two-tailed paired t-test; t_3 = 7.73, **p = 0.0045). Bottom left: significantly greater percentage of CRF vs. CCK BNST neurons co-expressing *Hcrt*-LH-RVdG (n=4 mice, two-tailed paired t-test; t_3 = 5.04, *p = 0.0151). Bottom right: significantly greater percentage of *Hcrt*-LH-RVdG-GFP+ neurons co-expressing CRF vs. CCK (n=4 mice, two-tailed paired t-test; t_3 = 3.81, *p = 0.0319). Centre and error bars are mean ± S.E.M. Abbreviations: ac; anterior commissure, ad; anterodorsal BNST, adl; anterodorsolateral BNST, adm; anterodorsomedial BNST, av; anteroventral BNST, jc; juxtacapsular nucleus, lv; lateral

ventricle, ov; oval nucleus, p; posterior BNST, pl; posterolateral BNST, pm; posteromedial BNST, vLS; ventral lateral septum. Scalebars: all 100 μm, except panel **d** (500 μm).

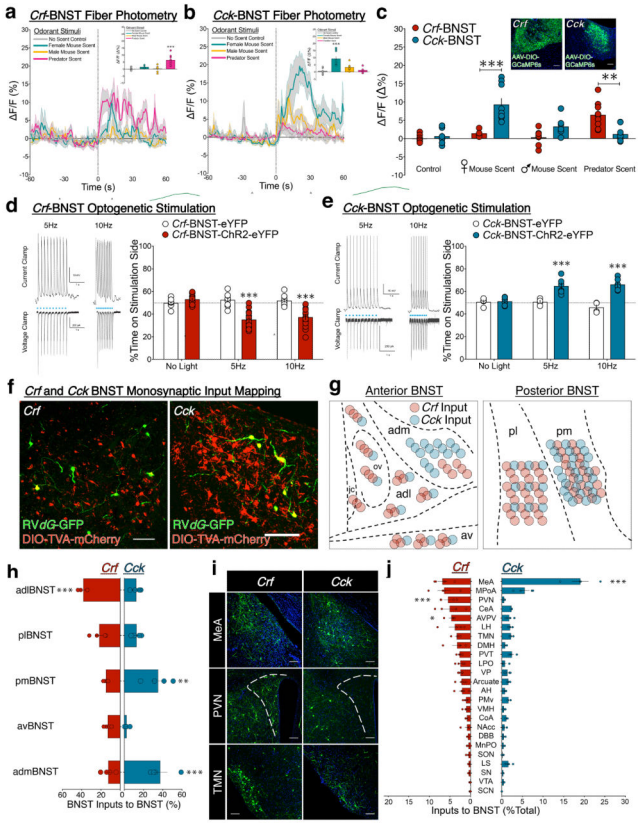

Figure 3. Crf and Cck BNST neurons for opposing emotional states

(a) Fluorescent Ca^{2+} activity traces from *in vivo* fiber photometry recordings of *Crf*-BNST neurons before and after (dashed line) exposure to salient odorant stimuli. Inset; mean fluorescence levels from *Crf*-BNST neurons during the 60s stimuli exposure phase (n=6 mice; 1–3 trials with each stimulus per subject, one-way ANOVA; $F_{3,24} = 13.33$, $p < 0.0001$, Bonferroni post-hoc comparison ***$p < 0.0001$ vs. no-scent control). **(b)** Fluorescent Ca^{2+} activity traces from *in vivo* fiber photometry recordings of *Cck*-BNST neurons before and after (dashed line) exposure to salient odorant stimuli. Inset; mean fluorescence levels from *Cck*-BNST neurons during the 60s stimuli exposure phase (n=6 mice; 1–3 trials with each stimulus per subject, one-way ANOVA; $F_{3,27} = 11.93$, $p < 0.0001$, Bonferroni post-hoc comparison ***$p = 0.0001$ vs. no-scent control). **(c)** Direct comparison of mean *Crf*-BNST and *Cck*-BNST fluorescence levels during the 60s stimuli exposure phase (n=6 *Crf* and n=6 *Cck*; two-way ANOVA; stimuli x BNST cell type interaction $F_{3,51} = 12.49$, $p < 0.0001$, *Crf* vs. *Cck* Bonferroni post-hoc comparisons **$p < 0.005$ ***$p < 0.0001$). **(d)** Left; *ex vivo* validation of ChR2-evoked spiking at 5Hz and 10Hz in *Crf*-BNST cell bodies. Right; *Crf*-BNST-ChR2 photostimulation is aversive in the RTPT (n=9 eYFP, n=15 ChR2-eYFP mice, two-way RM-ANOVA; ChR2 x stimulation interaction: $F_{2,44} = 22.63$, $p < 0.0001$, Bonferroni post-hoc comparisons ***$p < 0.0001$ vs. *Crf*-BNST-eYFP control group). **(e)** Left; *ex vivo* validation of ChR2-evoked spiking at 5Hz and 10Hz in *Cck*-BNST cell bodies. Right; *Cck*-BNST-ChR2 photostimulation is rewarding in the RTPT (n=4 eYFP, n=6 ChR2-eYFP mice, two-way RM-ANOVA; ChR2 x stimulation interaction: $F_{2,16} = 8.60$, $p = 0.003$, Bonferroni post-hoc comparisons ***$p < 0.0005$ vs. *Cck*-BNST-eYFP control group). **(f)**

Representative images of BNST starter cells co-expressing RV*dG*-GFP (green) and AAV5-DIO-TVA-mCherry (red) in *Crf* (left) and *Cck* (right) mice, replicated independently with similar results in four mice per group. **(g)** Visualization of relative abundance of BNST inputs onto *Crf* vs. *Cck* BNST neurons. **(h)** Quantification of BNST inputs onto *Crf* vs. *Cck* BNST neurons. (n=4 per group, two-way RM-ANOVA; BNST genetic subpopulation x BNST subdivision interaction: $F_{4,24} = 12.01$, $p < 0.0001$, Bonferroni post-hoc comparisons $^{**}p < 0.005$, $^{***}p < 0.0005$ vs. opposite genetic BNST subpopulation). **(i)** Representative images of upstream RV*dG*-GFP cells providing direct inputs onto *Crf* (left) or *Cck* (right) BNST neurons, replicated independently with similar results in four mice per group. **(j)** Quantification of relative abundance of brainwide inputs onto *Crf* vs. *Cck* BNST neurons (n=4 per group, two-way RM-ANOVA; BNST genetic subpopulation x input region interaction: $F_{23,138} = 10.76$, $p < 0.0001$, Bonferroni post-hoc comparisons $^{*}p < 0.05$, $^{***}p < 0.0001$ vs. opposite genetic BNST subpopulation). In panels a–e, h and j, centre and error bars are mean ± S.E.M. Scalebars: all 100 μm.

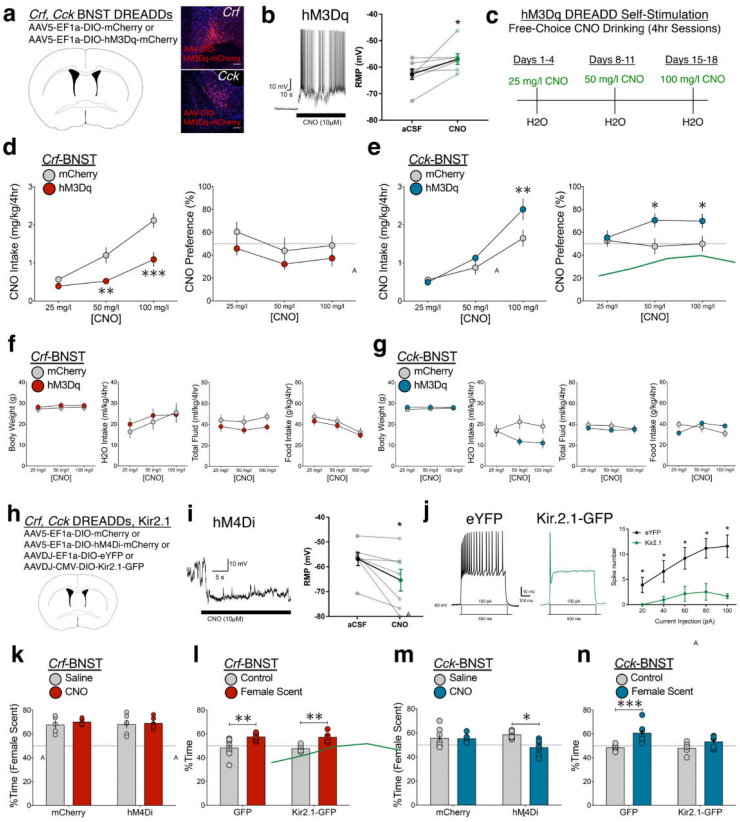

Figure 4. Crf and Cck BNST neurons: sufficiency and necessity for opposing motivated states

(a) *Crf*- and *Cck*-Cre mice received bilateral BNST infusion of either control (mCherry) or excitatory DREADD (hM3Dq) virus, replicated independently with similar results in six mice per group. **(b)** Relative to aCSF, CNO application to BNST neurons elicited robust spiking activity and increased membrane potential (n=7 neurons from two mice; two-tailed paired t-test; $t_6 = 2.49$, $^*p = 0.0472$). **(c)** Timeline for CNO drinking hM3Dq self-stimulation studies. **(d)** CNO intake (left) and CNO preference (right) in *Crf*-BNST-hM3Dq and control mice (n=6 *Crf*-mCherry, n=12 *Crf*-hM3Dq-mCherry mice, two-way RM-ANOVA; intake: DREADD x CNO interaction: $F_{2,32} = 5.32$, $p = 0.010$, Bonferroni post-hoc comparisons $^{**}p < 0.005$, $^{***}p < 0.0005$ vs. *Crf*-BNST-mCherry). **(e)** CNO intake (left) and CNO preference (right) in *Cck*-BNST-hM3Dq and control mice (n=15 *Cck*-mCherry, n=11 *Cck*-hM3Dq-mCherry mice, two-way RM-ANOVA; intake: DREADD x CNO interaction: $F_{2,48} = 5.41$, $p = 0.008$, Bonferroni post-hoc comparisons $^{**}p < 0.005$ vs. *Cck*-BNST-mCherry). **(f)** Body weight, water intake, total fluid intake, and food intake for *Crf* BNST mice in CNO drinking studies (n=6 *Crf*-mCherry, n=12 *Crf*-hM3Dq-mCherry mice, no significant group x CNO interactions two-way RM-ANOVA DREADD x CNO interaction; $p = 0.54, 0.52, 0.81, 0.96$). **(g)** Body weight, water intake, total fluid intake, and food intake for *Cck* BNST mice in CNO drinking studies (n=15 *Cck*-mCherry, n=11 *Cck*-hM3Dq-mCherry mice, no significant group x CNO interactions two-way RM-ANOVA DREADD x CNO interaction; $p = 0.62, 0.13, 0.69, 0.14$). **(h)** For chemogenetic inhibition experiments, *Crf*- and *Cck*-Cre mice received bilateral BNST infusion of either control (mCherry) or inhibitory DREADD (hM4Di) virus. For physiological inhibition experiments, *Crf*- and *Cck*-Cre mice received

bilateral BNST infusion of either control (eYFP) or inhibitory K+ channel (Kir2.1) virus. **(i)** Relative to aCSF, CNO application to hM4Di-expressing BNST neurons reduced spiking activity and significantly decreased resting membrane potential (n=7 neurons from two mice; two-tailed paired t-test; $t_6 = 2.59$, $*p = 0.0412$). **(j)** Relative to eYFP-expressing control BNST neurons, Kir2.1-infected BNST neurons showed reduced spiking activity in response to increasing current injection (n=5 neurons from two mice per group; Current x Virus interaction: $F_{4,32} = 3.1$, $*p = 0.029$, Bonferroni post-hoc comparisons $*p < 0.05$). **(k)** Behavioral approach to female mouse odorant stimuli in male *Crf*-BNST mice following hM4Di DREADD inhibition (n=5 *Crf*-mCherry, n=6 *Crf*-hM4Di-mCherry, two-way RM-ANOVA; DREADD x CNO interaction: $F_{1,9} = 0.12$, $p = 0.737$). **(l)** Behavioral approach to female mouse odorant stimuli vs. control no-scent stimuli in male *Crf*-BNST mice following Kir2.1 manipulation (n=8 *Crf*-GFP, n=6 *Crf*-Kir2.1-GFP mice, two-way RM-ANOVA; Kir2.1 x stimuli interaction: $F_{1,12} = 0.01$, $p = 0.912$, Bonferroni post-hoc comparisons $**p < 0.01$ vs. no-scent control). **(m)** Behavioral approach to female mouse odorant stimuli in male *Cck*-BNST mice following hM4Di DREADD inhibition (n=7 per group, two-way RM-ANOVA; DREADD x CNO interaction: $F_{1,12} = 4.98$, $p = 0.046$, Bonferroni post-hoc comparisons $*p < 0.05$ vs. saline control. **(n)** Behavioral approach to female mouse odorant stimuli vs. control no-scent stimuli in male *Cck*-BNST mice following Kir2.1 manipulation (n=8 per group, two-way RM-ANOVA; Kir2.1 x stimuli interaction: $F_{1,14} = 3.73$, $p = 0.074$, Bonferroni post-hoc comparisons $***p < 0.0005$ vs. no-scent control). In panels b, d–g, and i–n, centre and error bars are mean ± S.E.M. Scalebars: all 100 μm.

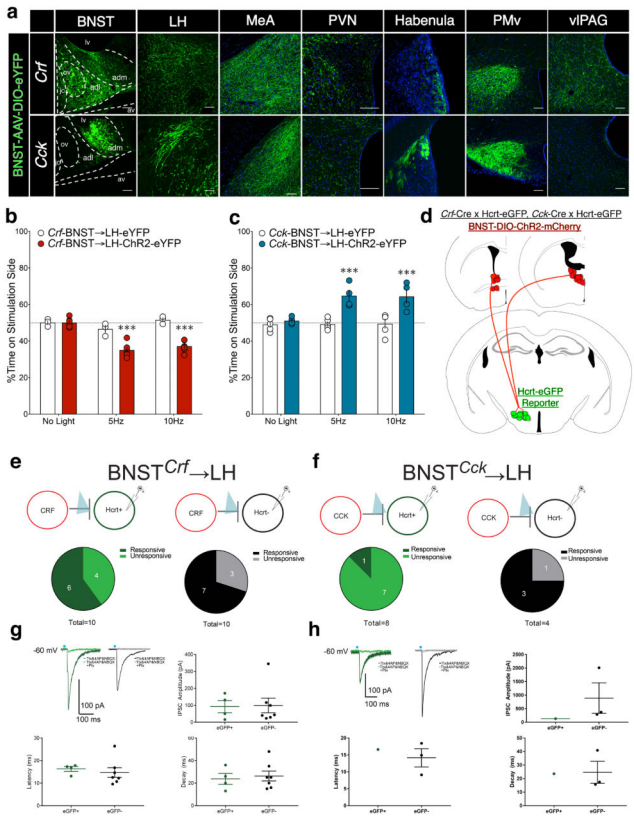

Figure 5. Crf and Cck BNST neurons: parallel LH pathways for opposing emotional states

(a) Representative images of AAV-DIO-eYFP expression in BNST cell bodies and downstream axonal fibers of *Crf* (top) and *Cck* (bottom) Cre mice, replicated independently with similar results in four mice per group. **(b)** *Crf*-BNST→LH photostimulation is aversive in the RTPT (n=3 *Crf*-BNST→LH-eYFP, n=6 *Crf*-BNST→LH-ChR2-eYFP mice, two-way RM-ANOVA; ChR2 x stimulation interaction: $F_{2,14} = 14.65$, $p = 0.0004$, Bonferroni post-hoc comparisons ***$p < 0.0001$ vs. *Crf*-BNST→LH-eYFP). **(c)** *Cck*-BNST→LH photostimulation is rewarding in the RTPT (n=5 *Cck*-BNST→LH-eYFP, n=4 *Cck*-BNST→LH-ChR2-eYFP mice, two-way RM-ANOVA; ChR2 x stimulation interaction: $F_{2,14} = 6.04$, $p = 0.013$, Bonferroni post-hoc comparisons ***$p < 0.0005$ vs. *Cck*-BNST→LH-eYFP). **(d)** Strategy for crossing Hcrt-eGFP reporter mice with *Crf* and *Cck* Cre mice, in order to inject AAV-DIO-ChR2-mCherry into BNST and record from Hcrt-eGFP+ and non-Hcrt-eGFP+ neurons in slice preparation. **(e)** *Crf*-BNST→LH slice recordings. 6/10 Hcrt-eGFP+ neurons and 7/10 non-Hcrt-eGFP+ neurons received direct synaptic input from *Crf*-BNST-ChR2 neurons. **(f)** *Cck*-BNST→LH slice recordings. 1/8 Hcrt-eGFP+ neurons and 3/4 non-Hcrt-eGFP+ neurons received direct synaptic input from *Cck*-BNST-ChR2 neurons. **(g)** Example traces showing 473nm blue light-evoked picrotoxin (Ptx)-sensitive inhibitory postsynaptic currents, indicating direct *Crf*-BNST-ChR2 connectivity onto Hcrt+ and non-Hcrt+ LH neurons, with no significant differences in IPSC amplitude, latency, or decay between responsive LH cell types (n=4 eGFP+, n=7 eGFP- cells). **(h)** Example traces showing 473nm blue light-evoked Ptx-sensitive inhibitory postsynaptic currents, indicating direct *Cck*-BNST-ChR2 connectivity in Hcrt+ and non-Hcrt

+ LH neurons, with no significant differences in IPSC amplitude, latency, or decay between responsive LH cell types (n=1 eGFP+, n=3 eGFP- cells). In panels b, c, g and h, centre and error bars are mean ± S.E.M. Scalebars: all 100 μm.